Refraction of Sound by Islands and Seamounts

W. H. MUNK

Institute of Geophysics and Planetary Physics, Scripps Institution of Oceanography, University of California, San Diego, La Jolla, California

F. ZACHARIASEN

California Institute of Technology, Pasadena, California

(Manuscript received 9 August 1990, in final form 3 January 1991)

ABSTRACT

We consider the propagation into shallow water of low-frequency and low-order acoustic modes trapped in the sound channel. The phase velocity slightly decreases and then increases with decreasing depth. This leads to an unusual pattern of wave refraction. Waves are "attracted" by islands and seamounts (rays turn toward shore) in "almost deep" water, and then are strongly "repelled" in shallow water. We examine the relative intensity of scattered arrivals in very long-range ocean transmissions. Forward scatter by islands and seamounts can give significant (order −10 dB) scattered arrivals, as can large-angle scatter (including backscatter) by large islands and by islands near the source or receiver. However, transmission of acoustic energy into the sea floor leads to loss of the scattered energy in the sound channel. Total reflection (no loss) is favored by glancing incidence on steep slopes of islands and seamounts with large compressional seismic velocities. We suggest a complementary relation between the intensities from an underwater explosion as recorded on axial hydrophones versus nearby land seismometers, with conditions favorable to reflection favoring hydrophones and vice versa. A preliminary attempt is made to compare measured and computed scattered intensities in the sound channel for operation WIGWAM (a deep-water nuclear explosion in 1955), operation CHASE, and the Perth to Bermuda transmission of 1960. Computed intensities are too low.

1. Introduction

An attempt to measure global ocean warming by very long [$O(10^4$ km)] acoustic transmissions has been proposed (Munk and Forbes 1989). Over such long ranges, there are a number of islands and a much larger number of seamounts that will scatter acoustic rays. Consequently the direct signal will be accompanied by scattered arrivals from different directions and at different times. We require some estimates of their intensity relative to the direct signal. If the scattered arrivals are of sufficient intensity, and if they are well separated in arrival time and/or azimuth, they provide welcome additional information about the horizontal structure of the ocean (much as vertical multipaths are used in ocean acoustic tomography to provide information about the vertical sound speed structure).

Scattering from islands and seamounts of acoustic energy from underwater explosions has been recognized since the early days of SOFAR experiments. The emphasis was on precise measurement of travel times; intensities were of minor concern provided the scattered arrival exceeded the detection threshold. We surmise that the scattering was usually visualized as a specular reflection from an underwater cliff or a Bragg-like reflection from a rough bottom, as sketched in the upper panels of Fig. 1.

An entirely different view emerges from consideration of the dispersion of sound waves in shallow water. Surprisingly, the phase velocity *increases* as the waves travel from deep into shallow water (ignoring for the moment a slight initial decrease), so that the waves are refracted *away* from shore, unlike the familiar refraction of (surface and internal) gravity waves *toward* shore (Fig. 1). At some depth $H^*(j, f)$ the phase velocity of acoustic mode j at frequency f becomes infinite: the wave cannot penetrate beyond this barrier depth.[1] Accordingly, acoustic waves are *repelled* by shallow water, whereas gravity waves are *attracted*. The refractive repulsion appears to be the dominant mechanism in coastal scattering.

A simple interpretation of the barrier depth follows from ray optics: a shoreward traveling ray is steepened at each collision with the sloping bottom until the ray becomes vertical at H^*. From a modal point of view,

Corresponding author address: Dr. Walter H. Munk, Inst. of Geophysics and Planetary Physics, A-025, Scripps Institution of Oceanography, La Jolla, CA 92093-0225.

[1] In fact the coastal turning point is generally at some depth slightly larger than H^* where the phase velocity is large but not infinite.

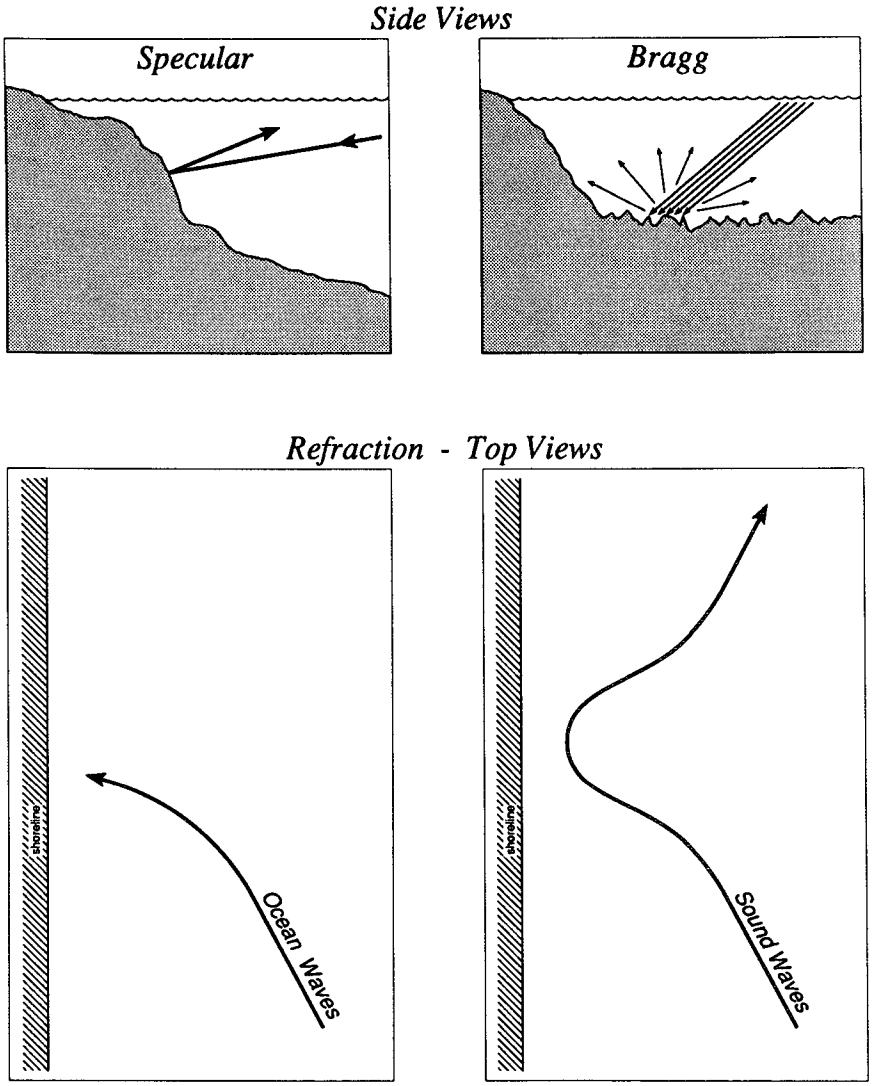

FIG. 1. The upper panels illustrate two possible mechanisms of coastal scatter: specular reflection from steep cliffs, and Bragg scatter from a rough sea floor. The left lower panel illustrates the familiar refraction of gravity waves (surface and internal) advancing into shallow water, with the rays turning toward the shore normal (as if attracted by shallow water), and the wave crests (not shown) aligned increasingly parallel to shore. Acoustic modes (right lower panel) are initially attracted as in the case of gravity waves, but then strongly repelled by shallow water.

the oscillatory wavefunction is compressed between top and bottom until the vertical wavelength is reduced to the acoustic wavelength and can be compressed no further. The offshore distance x^* where $H(x^*) = H^*$ is the WKBJ turning point of a horizontal wavefunction, which is oscillatory seaward of x^* and exponentially damped shoreward of x^*.

The pioneering paper on submarine echoes (Luskin et al. 1962) is a remarkable tribute to the intuition of the early workers at the Lamont Geological Observatory of Columbia University, under the leadership of Maurice Ewing and J. Worzel. The authors quote Ewing and Worzel as observing echoes from CAT Island in 1945 with a 100-s delay at the Eleuthera Island SOFAR station. Ewing predicted that a 4-pound explosive charge could be recorded at a range of at least 10 000 miles. In 1951 submerged 50–300-pound detonations in the area between Puerto Rico and Bermuda were recorded by Gordon Hamilton at the Columbia University Geophysical Field Station in Bermuda (Luskin et al. 1962). The authors' interpretation of the many echoes recorded had it all straight, "Sound rays impinging on a sloping bottom that rises to the ocean surface can be reflected from the bottom and the surface until an angle of incidence is obtained with either the bottom or the surface which reverses their direction of

travel. Obviously, the steeper the slope, the fewer top and bottom reflections before the required incidence is obtained to make the rays reverse direction in a horizontal sense. Hence, a gently inclined slope must extend much nearer the surface than a steep one in order to produce an echo." The reflector positions for recorded indirect arrivals were calculated and correspond to submarine structures with steep bottom slopes, including several known seamounts and one uncharted seamount.

The term "horizontal refraction" was introduced by Weston (1961). A treatment of sound waves along a straight coastline in very shallow water is given by Brekhovskikh and Lysanov (1982) under the heading of a "coastal wedge." They refer to earlier work by Harrison (1977) who treats the cases of basins, troughs, ridges, and seamounts. The basic treatment stems from the work of J. B. Keller and was first applied to underwater acoustic propagation by Weinberg and Burridge (1974). Some pertinent observations have recently been reported by Doolittle et al. (1988). In these papers the acoustic waveguide is determined by the surface and bottom boundaries of the coastal wedge, with the sound speed profile $C(z)$ playing a negligible role (as if C were constant). The reverse holds in deep water: there the well-known SOFAR waveguide is associated with a minimum in $C(z)$, and the boundaries play a negligible role. Our contribution is to combine the shallow- and deep-water asymptotes into a single formalism. This leads to some interesting results.

The present treatment is linear. McDaniel (1982) and others have claimed significant mode coupling over a sloping bottom, but Desaubies and Dysthe (personal communication) find very little mode coupling.

Scattering intensity depends on many considerations: on the global geometry of source, receiver, and scatterer; on the local scatter geometry (island diameter, seamount depth, bottom slope); and on acoustic frequency and modal decomposition. A pleasing result is that the role played by each of these parameters is amenable to quantitative estimates.

2. Wave dispersion

The phase velocity of an acoustic wave depends on mode number n, frequency f, as well as on the vertical profile of sound speed $C(z)$. An adiabatic treatment of the "wedge problem" has been given by Brekhovskikh and Lysanov (1982) and by Doolittle et al. (1988). These authors considered an acoustic mode traveling up a sloping beach with depth $H(x)$. The modal wavefunction is vertically compressed until the waves reach a depth H^* where the vertical wavelength equals the acoustic wavelength. For a free surface ($p = 0$) and a rigid bottom ($dp/dz = 0$)

$$H^*(j,f) = \frac{(j + \tfrac{1}{2})C}{2f}, \quad j = 0, 1. \tag{1}$$

At this point, phase velocity c is infinite (phase slowness $s = 1/c$ is zero) and the waves cannot penetrate beyond this "barrier depth." In ray language, each "collision" with the sloping bottom steepens the rays, until the rays become vertical at H^*. An appropriate asymptotic representation is given by

$$\frac{s^2(H)}{s_\infty{}^2} = 1 - \frac{H^{*2}}{H^2}. \tag{2}$$

In this limit the sound speed profile $C(z)$ plays a negligible role and the sound speed might as well be taken as constant; the change in phase velocity is entirely the result of the converging surface and bottom boundaries.

In the other limit of very deep water, the boundaries play a negligible role and the wave guide is entirely determined by the sound channel $C(z)$. Dashen and Munk (1990) have given a general solution that connects the two limits. Details depend in a complex way on the form of the sound channel $C(z)$, but there are two generic features: 1) in very shallow water the phase velocity approaches the form (2); 2) in "almost deep" water, phase velocity is slightly *less* than the deep-water velocity and approaches the deep water velocity c_∞ exponentially with increasing depth. A minimum occurs where the lower WKBJ turning point of the acoustic mode intersects the sloping sea bottom. For low modes this occurs near the depth of the sound axis H_{AX}.

We choose to represent this behavior in terms of the squared sound slowness:

$$\frac{s^2(H)}{s_\infty{}^2} = 1 - \gamma^{-2} + ae^{-b\gamma}, \quad \gamma(H) = \gamma^* \frac{H}{H^*}. \tag{3}$$

The three constants a, b, γ^* are evaluated from the requirements that

$$s(H^*) = 0, \quad s(H_m) = \text{maximum} = s_\infty\sqrt{1 + \sigma}.$$

The result is

$$a = \frac{2}{b}\gamma_m{}^{-3}e^{b\gamma_m}, \quad b = \frac{2}{\gamma_m(1 + \sigma\gamma_m{}^2)},$$

$$\gamma_m = \gamma^* \frac{H_m}{H^*}. \tag{4}$$

We consider three cases

1) $\sigma = 0$, $a = 0$, $\gamma^* = 1$,

2) $\sigma = 0.005$, $a = 0.01e$, $b = \sqrt{0.005}$, $\gamma^* = 0.9876$, $H_m/H^* = 14.32$

3) $\sigma = 0.04$, $a = 0.08e$, $b = \sqrt{0.04}$, $\gamma^* = 0.920222$, $H_m/H^* = 5.43$.

The first case reduces to Eq. (2) without a maximum in s^2. The second case $\sigma = 0.005$ gives a fair fit to $s(H)$ for an Airy-type sound channel (Dashen and Munk 1990, Fig. 5). The third case $\sigma = 0.04$ has an exagger-

ated maximum and is chosen for clarity of the illustrations (Fig. 2 and subsequent figures). The numerical values correspond to a one-dimensional model

$$\frac{H_m}{H^*} = \frac{1}{\gamma^* \sigma^{1/2}}, \quad a = 2\sigma e, \quad b = \sigma^{1/2}.$$

For very large H/H^* the second term in Eq. (3) dominates over the third term, and this leads to a nonphysical s^2 minimum beyond the maximum. This minimum can be kept negligibly small by an appropriate choice of constants.

3. Refracted rays

The ray path is determined by Fermat's principle that the travel time $\int s(r)dl$ be a minimum:

$$\delta \int s(r)dl = 0 \tag{5}$$

with the integral taken along the ray path. Using cylindrical coordinates (Fig. 3), Euler's equation for the ray $r(\alpha)$ is obtained from (5) and (after some manipulation) can be written

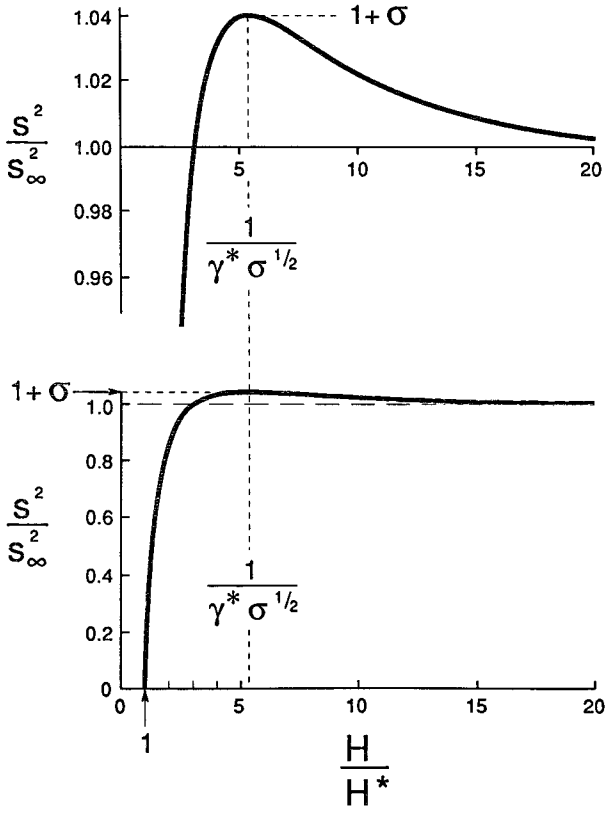

FIG. 2. The squared phase slowness for $\sigma = 0.04$. The maximum value $s_m^2/s_\infty^2 = 1 + \sigma = 1.04$ occurs at $H = H_m = (\gamma^*\sigma^{1/2})^{-1}H^*$. The slowness vanishes ($c^* = \infty$) at the barrier ($H = H^*$).

$$\frac{d}{d\alpha}\left(\frac{1}{r}\frac{dr}{d\alpha}\right) - 1 - \frac{1}{r}\left[r^2 + \left(\frac{dr}{d\alpha}\right)^2\right]\frac{1}{s(r)}\frac{ds(r)}{dr} = 0. \tag{6}$$

The boundary conditions are that

$$x \to -\infty, \quad y \to y_{\text{in}} \quad \text{as} \quad \alpha \to \pi$$
$$x \to +\infty, \quad y \to \pm\infty \quad \text{as} \quad \alpha \to \alpha_\infty, \tag{7}$$

where α_∞ is the *total* angle through which the ray is turned as a result of the island encounter and y_{in} is the value of y of the incident rays, i.e., the "impact parameter."

Equation (6) can be integrated once to give

$$rs(r)\left[1 + \left(\frac{1}{r}\frac{dr}{d\alpha}\right)^2\right]^{-1/2} = \text{constant} \tag{8}$$

which is Snell's law in cylindrical coordinates. At the limit $x \to -\infty$ we have $s(r) = s_\infty$ and since $y_{\text{in}} = r \times \sin\alpha$, this gives $y_{\text{in}}s_\infty$ for the constant in (8). Accordingly, Eq. (8) can be written

$$\frac{d\alpha}{dr} = \frac{1}{r}\left\{\left[\frac{rs(r)}{y_{\text{in}}s_\infty}\right]^2 - 1\right\}^{-1/2}. \tag{9}$$

The point of closest approach of the refracted ray is designated by $\hat{r}$, $\hat{\alpha}$. At this point $dr/d\alpha = 0$ and hence

$$\hat{r}\hat{s} = y_{\text{in}}s_\infty \tag{10}$$

where $\hat{s} = s(\hat{r})$. We write (9) in the final form

$$\frac{d\alpha}{dr} = \frac{1}{r}\left\{\left[\frac{rs(r)}{\hat{r}\hat{s}}\right]^2 - 1\right\}^{-1/2} \tag{11}$$

and introduce the notation

$$F(r) = \int_{\hat{r}}^{r} \frac{dr}{r}\left\{\left[\frac{rs(r)}{\hat{r}\hat{s}}\right]^2 - 1\right\}^{-1/2}. \tag{12}$$

The angle α diminishes from its initial value π to a final value α_∞; $\hat{\alpha}$ is midway:

$$\hat{\alpha} = \frac{1}{2}(\pi + \alpha_\infty) \tag{13}$$

and

$$\alpha(r) = \hat{\alpha} \mp F(r) \tag{14}$$

with the upper sign corresponding to the orbit *after* the closest approach. Thus,

$$\alpha_\infty = \hat{\alpha} - F_\infty, \tag{15}$$

which together with (13) yields

$$\hat{\alpha} = \pi - F_\infty, \quad \alpha_\infty = \pi - 2F_\infty. \tag{16}$$

We now require the bottom profile $H(r)$. The simplest case is that of a constant slope μ;

$$H = H_0 + \mu r \quad \text{or} \quad H = \mu(r - r_0), \quad r \geq r_0 \tag{17}$$

where $H_0 = -\mu r_0$ is negative for conical islands and

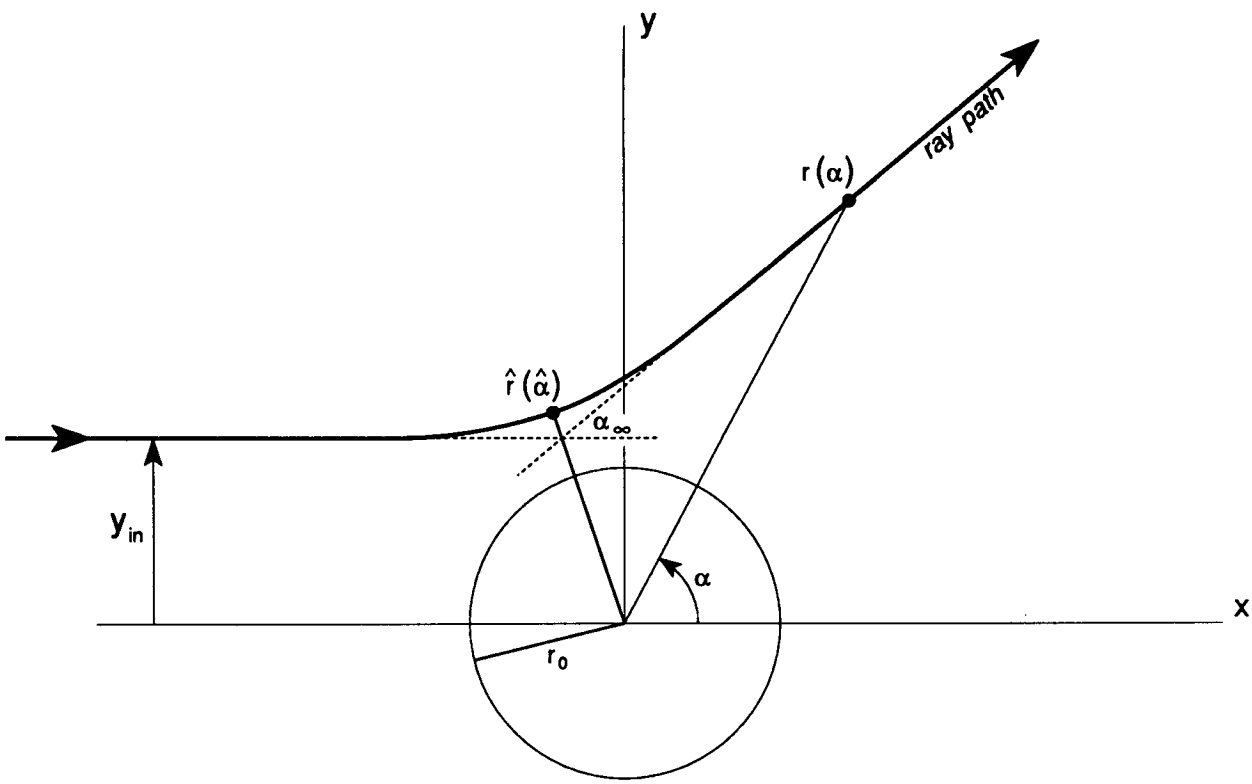

FIG. 3. An incident ray travels in the positive x direction along $y = y_{in}$ prior to interacting with the island (y_{in} is also called the "impact parameter"). Following interaction the ray is turned through an angle $\alpha_\infty(y_{in})$. The refracted ray path $r(\alpha)$ has a point of closest approach $\hat{r} = r(\hat{\alpha})$. A positive scatter ($\alpha_\infty > 0$) corresponds to a repelled ray (as shown), a negative α_∞ to an attracted ray. A distant receiver may receive a positive scatter from the "north" side of the island and a negative scatter from the "south' side.

positive for conical seamounts. It is convenient to define

$$Z_0 = +\mu r_0 \tag{18}$$

as the elevation above sea level of the cone summit (negative for seamounts). Write

$$H^* = \mu(r^* - r_0), \quad \hat{H} = \mu(\hat{r} - r_0),$$
$$H_m = \mu(r_m - r_0) \tag{19}$$

for the depths of the barrier, of the point of closest approach and of maximum phase slowness, respectively. We normalize all radii by dividing with (H^*/μ), the distance offshore of the barrier. Thus, $R = r(H^*/\mu)^{-1}$; in particular

$$R_0 = Z_0/H^*, \quad R^* = R_0 + 1,$$
$$\hat{R} = R_0 + \hat{H}/H^*, \quad R_m = R_0 + H_m/H^*. \tag{20}$$

The value R_0 is negative for seamounts. [A more standard procedure would be to normalize relative to the island radius r_0 (say), but this would call for a different procedure for islands and seamounts.]

Equations (3) and (10) give the expression for the normalized impact parameter

$$Y = y_{in}(H^*/\mu)^{-1} = \hat{R}[1 - \hat{\gamma}^{-2} + ae^{-b\hat{\gamma}}]^{1/2},$$
$$\hat{\gamma} = \gamma^*\hat{H}/H^* = \gamma^*(\hat{R} - R_0). \tag{21}$$

This is shown in Fig. 4 for various values of $R_0 = Z_0/H^*$. At very large Y, $\hat{H}/H^* \to \infty$ and $Y \to \hat{R}$. At small Y one needs to distinguish between islands and shallow seamounts on one hand, and "deep seamounts" on the other hand. For normal impact $Y = 0$, waves are totally reflected ($\alpha_\infty = \pi$), whereas for deep seamounts the waves pass right over the summit without deflection ($\alpha_\infty = 0$).

To consider this critical case in more detail, we might as well simplify the problem by setting $a = 0$ and thus ignoring the slight $c(r)$ minimum. Then for $Y = 0$ we have $\hat{\gamma} = 1$ and hence $\hat{H} = H^*/\gamma^*$. The critical case is not for the point island $Z_0 = 0$, nor a seamount at the barrier depth $Z_0 = -H^*$ (where $c = \infty$), but slightly deeper at $Z_0 = -H^*/\gamma^*$ where $c(\hat{r})$ is large enough (but not infinite) to give total reflection. (The numerical difference between H^* and H^*/γ^* is insignificant.) Accordingly, with $Y = 0$,

$$\alpha_\infty = \begin{pmatrix} 0 \\ \pi \end{pmatrix} \quad \text{for} \quad Z_0/H^* = R_0 = -1/\gamma^* \pm \epsilon.$$

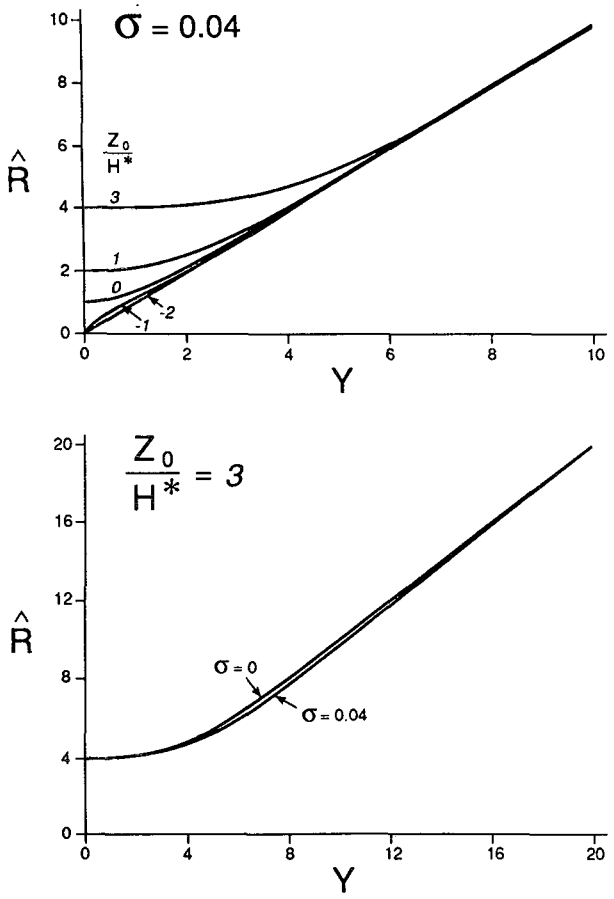

FIG. 4. The radius of closest approach $\hat{R}$ versus the impact parameter Y, for islands ($R_0 = Z_0/H^* > 0$) and seamounts ($R_0 < 0$). Waves passing far from the islands or seamounts are not appreciably refracted and $\hat{R} \approx Y$. Curves are for $\sigma = 0.04$, but depend only weakly on σ (lower panel).

It follows that

$$\hat{R}(0) = R_0 + 1/\gamma^* \quad \text{for} \quad R_0 > -1/\gamma^*,$$
$$\hat{R}(0) = 0 \quad \text{for} \quad R_0 < -1/\gamma^*.$$

We need to chose numerical parameters. The slope may vary from $\mu = 0.01$ at some continental borders to $\mu = 0.2$ for steep islands and seamounts. For H^* we concentrate on low modes and low frequencies

$$H^* = \frac{j + 1/2}{2fS} = \quad 38 \text{ m} \quad 412 \text{ m} \quad 7.5 \text{ m} \quad 82 \text{ m}$$

for $j, f = 0$, 10 Hz 5, 10 Hz 0, 50 Hz 5, 50 Hz.

For orientation, we choose

$$\mu = 0.05, \quad H^* = 0.1 \text{ km}, \quad H^*/\mu = 2 \text{ km}.$$

Figure 5 shows the refraction pattern for the six cases with parameters given in Table 1. The first case corresponds to a relatively large island (radius $r_0 = 6$ km). The barrier radius $r^* = 8$ km (where $c = \infty$) is 2 km offshore at a depth $H^* = 0.1$ km. The radius of minimum phase velocity is $r_m = 16$ km. Rays with impact parameters $Y = 0, 1, \ldots, 10$ ($y_{in} = 0, 2, \ldots, 20$ km) are drawn. Those outside of r_m are always attracted *toward* the island (negative α_∞, see Fig. 3). For Y less than 7 the rays are largely repelled. As $Y \to 0$, $\alpha \to +\pi$ (backscatter) and $\hat{r} \to r^*$. For the point island ($Z_0 = 0$, $r_0 = 0$) the domain of forward scatter with refraction toward the island is increased. For the critical case $R_0 = -1/\gamma^*$ there is backscatter at $Y = 0$ for $Z_0/H^* = -1/\gamma^* + \epsilon$ and forward scatter for $Z_0/H^* = -1/\gamma^* - \epsilon$. For $Z_0/H^* = R_0 = -H_m/H^* = -5$ we have $r_m = 0$ and the rays are refracted toward the island for all Y, albeit by a small angle.

The "caustic" drawn through the points of closest approach $\hat{r}(\alpha)$ determines the boundary of the geometric shadow cast by the island. This is the high wavenumber limit of the wave solution, which shows diffractive penetration of the wave shadow. Buckingham (1986) and Buckingham et al. (1986) give the wave solution for the case $r_0 = 0$.

The curves are generated as follows. For a specified Z_0/H^* and Y, we have from (20) $\hat{H}/H^* = \hat{R} - R_0 = \hat{R} - Z_0/H^*$; substituting into (21) we solve numerically for $\hat{R}$ as a function of Z_0/H^* and Y. The integrand of (12) is written as a function of the parameter $\rho = r/\hat{r}$ and the integration is performed numerically from perigee ($\rho = 1$) to any point $\rho_u = r_u/\hat{r}$:

$$F(r_u) = \int_1^{\rho_u} \frac{d\rho}{\rho} \left\{ \left[\frac{\rho s(\rho)}{s(1)} \right]^2 - 1 \right\}^{-1/2}, \tag{22}$$

$$\left[\frac{s(\rho)}{s(1)} \right]^2 = \frac{1 - \gamma^{-2} + a \exp(-b\gamma)}{1 - \hat{\gamma}^{-2} + a \exp(-b\hat{\gamma})} \tag{23}$$

$$\gamma = \gamma^*(\rho\hat{R} - R_0), \quad \hat{\gamma} = \gamma^*(\hat{R} - R_0). \tag{24}$$

The ray equation then follows from (14) and (16):

$$\alpha(r) = \pi - F_\infty \mp F(r). \tag{25}$$

4. Scattering angle

Figure 5 is drawn for visualization of the nearshore refraction. From now on all that is required is the far-field relation $\alpha_\infty(Y)$ which is found directly from (16). To avoid apparent divergences at the lower limit, it is convenient to absorb π into the integral, so that

$$\alpha_\infty = 2 \int_{\hat{r}}^{\infty} \frac{dr}{r} \left\langle \left\{ \left(\frac{r}{\hat{r}} \right)^2 - 1 \right\}^{-1/2} - \left\{ \left[\frac{r}{\hat{r}} \frac{s(r)}{\hat{s}} \right]^2 - 1 \right\}^{-1/2} \right\rangle. \tag{26}$$

Set $r = \hat{r} \sec\upsilon_1$, $sr = \hat{s}\hat{r} \sec\upsilon_2$, hence $\sec\upsilon_2 = (s/\hat{s}) \sec\upsilon_1$. The angle υ_1 increases monotonically from 0 to $\pi/2$ with the angle between r and $\hat{r}$ (Fig. 3). Then using (23), (24), and $\rho = \sec\upsilon_1$, the integral reduces to

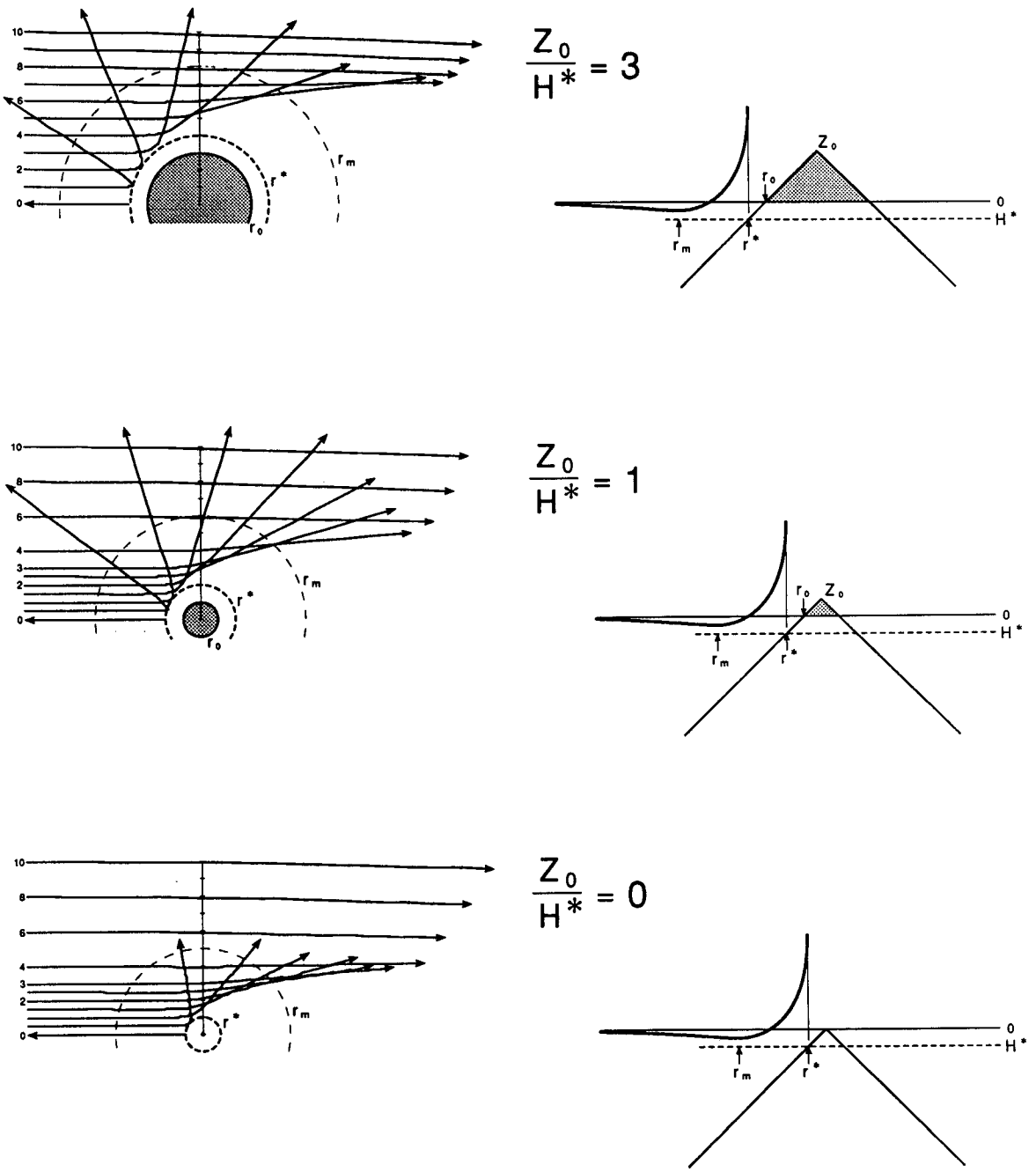

FIG. 5. Top view (left) and a side view (right) for refraction by islands and seamounts, for the parameters listed in Table 1. Phase velocity $c(r)$ is plotted to the right, going from $c(r^*) = \infty$ to a minimum $c(r_m)$ to an offshore asymptotic $c_\infty = c(\infty)$. The island radius r_0, barrier radius r^*, and radius of minimum phase velocity r_m are shown.

$$\alpha_\infty = 2\int_0^{\pi/2}\left[1 - \frac{\tan(\upsilon_1)}{\tan\upsilon_2(\upsilon_1)}\right]d\upsilon_1. \qquad (27)$$

This is plotted in Fig. 6. Again note that $\alpha_\infty(0) = \pi$ for $Z_0/H^* > -1/\gamma^*$ and $\alpha_\infty(0) = 0$ for $Z_0/H^* < -1/\gamma^*$. The upper panels show the relation for forward scatter ($\alpha_\infty \ll 1$) in more detail. For $-1/\gamma^* < Z_0/H^* < -5$, there is both a positive (repulsive) and negative (attractive) extremum. For $Z_0/H^* < -5$, α_∞ is negative at all Y. Dashed curves connecting the extrema are the important caustics (see also Fig. 9).

5. Ray divergence

An important parameter is the ray divergence $d\alpha_\infty/dY$. Clearly the scattered intensities are small if neighboring incident rays (small δY) are scattered into

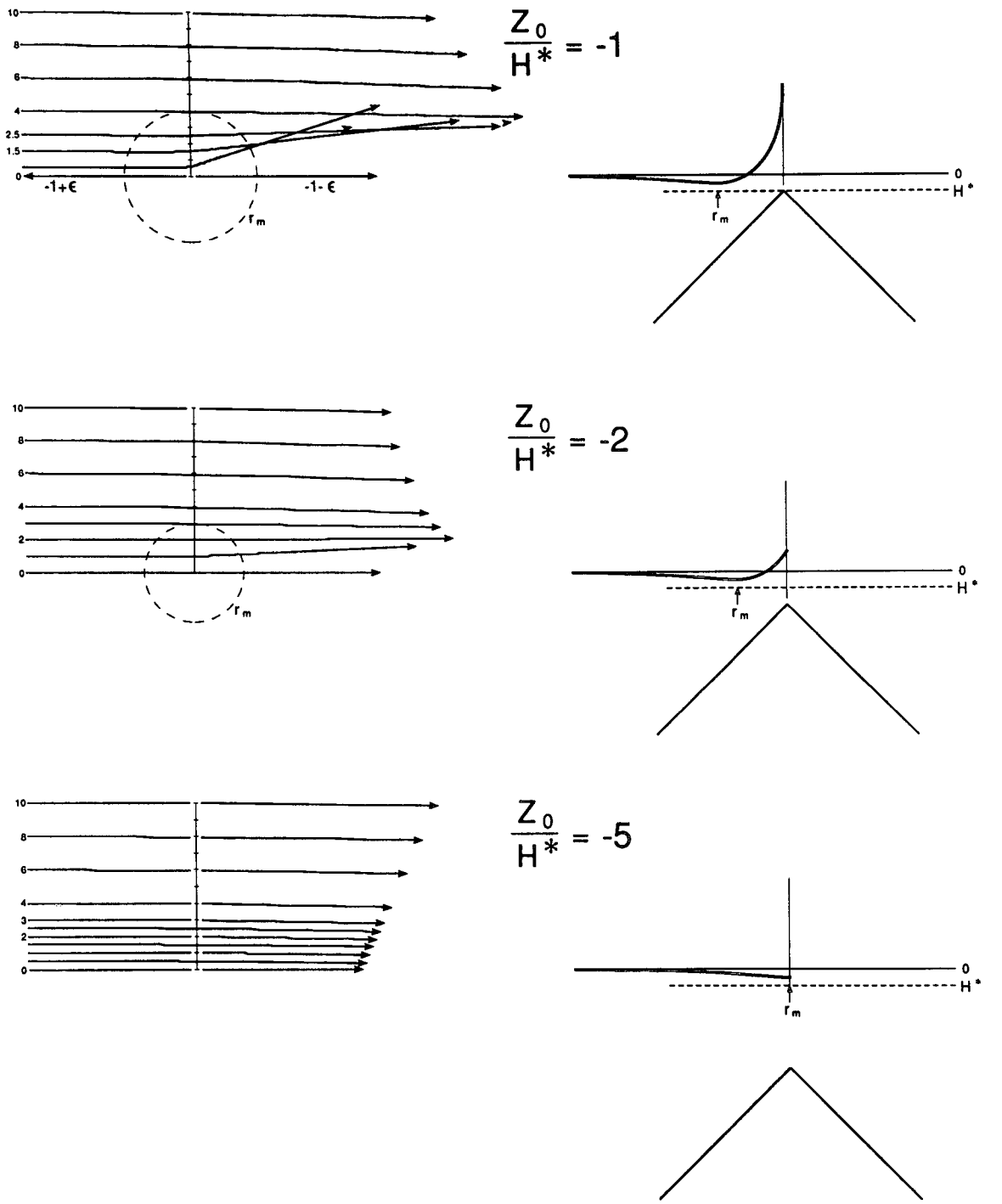

FIG. 5. (*Continued*)

widely differing directions (large $\delta\alpha_\infty$). Thus, large intensities are associated with small $|d\alpha_\infty/dY|$. (A quantitative discussion of scattered intensities follows in §7.)

From an inspection of Fig. 6, we see that there are three regimes of small ray divergence: 1) very small-angle attractive (negative α_∞) forward scatter for large Y. This would apply for scatterers almost on the direct acoustic path. 2) Small-angle forward scatter associated with the negative extrema of α_∞. We refer to this as the "attractive caustic". 3) Small-angle forward scatter associated with positive maxima of α_∞, the repulsive caustic. The latter exists only for seamounts in the range $-5 < Z_0/H^* < -1$. In contrast, large-angle scatter

TABLE 1. Parameters for Fig 5, using $H^*/\mu = 2$ km, $H_m/H^* = 5$, and $\sigma = 0.04$.

	Islands			Seamounts		
$R_0 = Z_0/H^*$	3	1	0	−1	−2	−5
$R^* = R_0 + 1$	4	2	1	0	(−1)	(−4)
$R_m = R_0 + H_m/H^*$	8	6	5	4	3	0

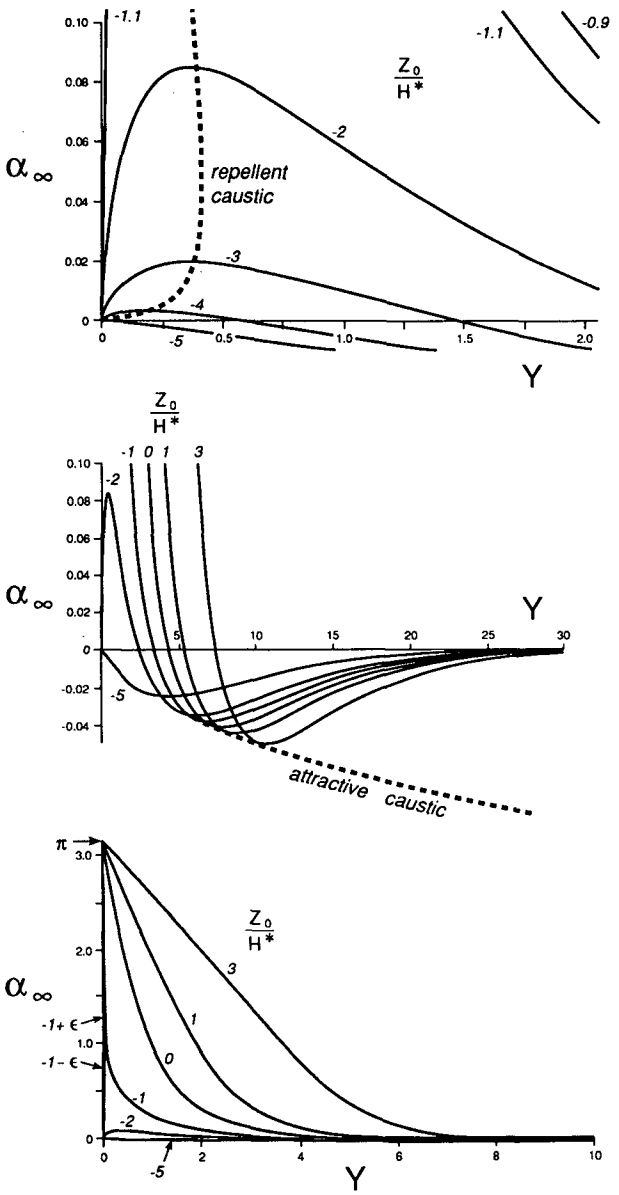

FIG. 6. The scattering angle as function of $Y = y_{in}(H^*/\mu)^{-1}$ for indicated values of Z_0/H^* and $\sigma = 0.04$. (See Fig. 3 for definitions). The upper panels show the situation for forward scatter ($\alpha_\infty \ll 1$) in more detail. Dashed curves designate the caustics along which $d\alpha_\infty/dY = 0$.

(including backscatter) is associated with large ray divergence.

For a fixed location of source, receiver and scatterer, the required scattering angle α_∞ is known. It is then convenient to compute the dispersion $d\alpha_\infty/dY$ as a function of the "global coordinate" α_∞ rather than the "local" coordinate Y (Fig. 7). To derive this relation it is convenient to compute

$$\alpha_\infty, \quad d\alpha_\infty/d\hat{R}, \quad dY/d\hat{R}$$

as functions of $\hat{R}$, using the relations already derived and to obtain $d\alpha_\infty/dY$ by a division of the last two terms.

6. Asymptotics

We require asymptotic relations for the interpretation and extrapolation of the foregoing results.

a. Point Island $Z_0 = 0$ and $\sigma = 0$

From (22),

$$F_\infty = (1 - \gamma^{*-2}\hat{R}^{-2})^{1/2} \int_1^\infty \frac{d\rho}{\rho(\rho^2 - 1)^{1/2}}$$

$$= (1 - \gamma^{*-2}\hat{R}^{-2})^{1/2} \frac{\pi}{2} = \frac{Y}{\hat{R}} \frac{\pi}{2}$$

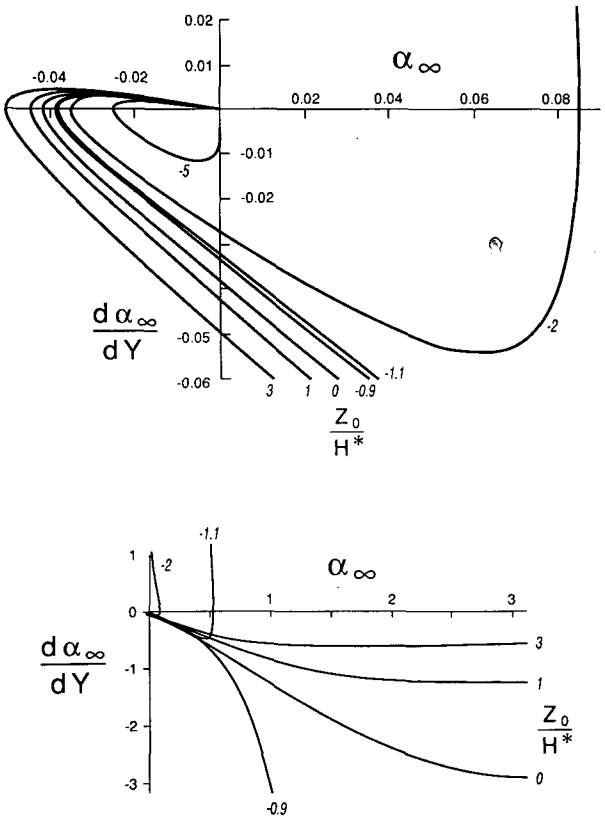

FIG. 7. The ray divergence $d\alpha_\infty/dY$ as function of the scattering angle α_∞. The intensity is proportional to $1/|d\alpha_\infty/dY|$.

so that

$$\alpha_\infty = \pi - 2F_\infty = \pi(1 - Y/\hat{R}). \quad (28)$$

For small Y, $\hat{R} = 1$ and $\alpha_\infty = \pi(1 - Y)$, which is a good approximation for α_∞ between π (backscatter) and $\pi/2$. For large Y, $\hat{R} \to Y$ and $\alpha_\infty \to 0$.

b. Near forward scatter, $\alpha_\infty \ll 1$

For weak scattering, the phase velocity $c(r)$, and hence the slowness $s(r)$, differ little from a constant. So let us write $s^2(r) = s_\infty{}^2 + \delta s^2(r)$ and expand (26) to first order in δs^2:

$$\alpha_\infty = \int_{\hat{r}}^{\infty} \frac{\hat{r}rdr}{(r^2 - \hat{r}^2)^{3/2}} \frac{[\delta s^2(r) - \delta s^2(\hat{r})]}{s_\infty{}^2}. \quad (29)$$

With the choice (3) for the slowness, the integral in (29) may be evaluated analytically. The result is

$$\alpha_\infty = \frac{1}{\gamma^{*2}} \frac{R_0\hat{R}(R^* - R_0)^2}{(\hat{R} - R_0)^2(\hat{R} + R_0)^2} \times \left\{3 + \frac{\hat{R}^2 + 2R_0{}^2}{R_0(|\hat{R}^2 - R_0{}^2|)^{1/2}} \times \left[\frac{\pi}{2} + \tan^{-1}\frac{R_0}{(|\hat{R}^2 - R_0{}^2|)^{1/2}}\right]\right\} - a\exp(\gamma^* bR_0)\gamma^* b\hat{R}K_0(\gamma^* b\hat{R}) \quad (30a)$$

for $\hat{R}^2 > R_0{}^2$, while for $\hat{R}^2 < R_0{}^2$, replace $[\pi/2 + \tan^{-1}R_0(\hat{R}^2 - R_0{}^2)^{-1/2}]$ by

$$\ln\frac{-\hat{R}}{R_0 + (R_0{}^2 - \hat{R}^2)^{1/2}}. \quad (30b)$$

The latter formula applies to seamounts for small Y. In both cases the first term comes from the "repulsive core" in (3), whereas, the last term is due to the outer exponential "attractive shell." The term K_0 is the conventional Bessel function of imaginary argument. We may also remark that to lowest order, it is sufficient to replace the point of closest approach $\hat{R}$ in (30) by the impact parameter Y. Figure 8 shows the very close agreement between (27) and (30).

For small impact parameters, the first terms in (30) dominate, and the island or seamount repels the ray. For large impact parameters, the Bessel function term resulting from the exponential in (3) wins, and the rays are attracted (albeit always weakly) to the island or seamount. Both of these effects are visible in Fig. 5. (For sufficiently deep seamounts, as mentioned earlier, the repulsion disappears, and only the weak attraction remains. This case is shown in the last drawing of Fig. 5.)

The dashed curves in Fig. 6 show the maximum negative deflections for islands, and the maximum positive deflections for seamounts. These curves are constructed from Eq. (30) by setting $d\alpha_\infty/dY = 0$, thus, yielding

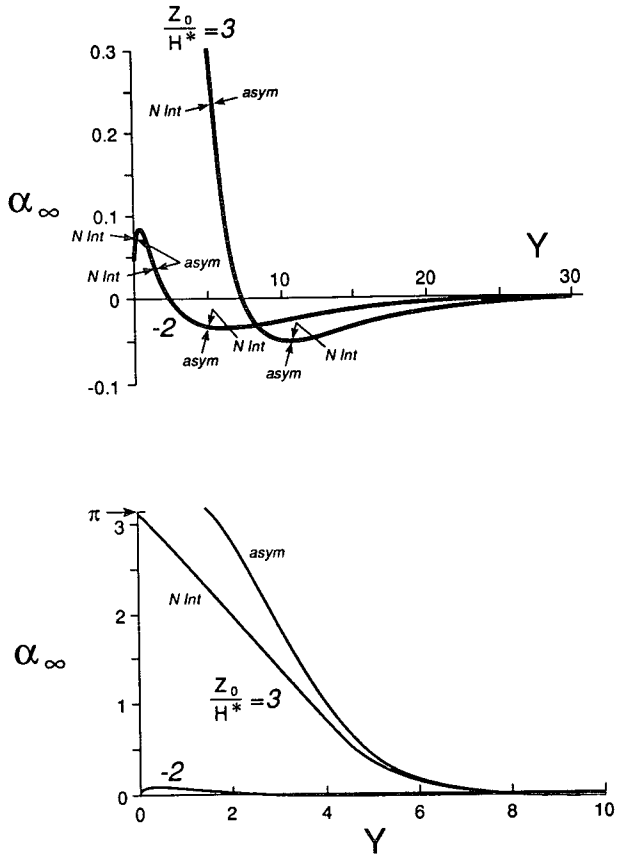

FIG. 8. Comparison of numerical integration (27) with asymptotic solution (30) for $Z_0/H^* = -2$ and $+3$. For forward scatter (small α_∞, upper figure) the solutions are too close to be shown separately, and we indicate which of the solutions is above or beneath.

$$\min\alpha_\infty(R_0) \quad \text{and} \quad \max\alpha_\infty(R_0) \quad (31)$$

as shown in Fig. 9. These are known as caustics, and they represent conditions of maximum intensity. The curves represent the "illustrative" value $\sigma = 0.04$ and the "realistic" value of $\sigma = 0.005$ for which the parameters were listed following Eq. (4).

For the negative (attractive) caustic the realistic σ yields maximum deflections of less than 1° for even quite large islands. The repellent caustic, however, can lead to large deflections for seamounts extending upwards to near H^*, and these deflections depend only weakly on σ. The case $\sigma = 0.005$ gives a somewhat larger deflection. In fact, if the attractive term (30b) is neglected, the result is $\max(\alpha_\infty) = 0.47R_0{}^{-2}$ at $\hat{R} = 0.30(-R_0)$.

c. Near backward scatter

As we see from (16), this is the case of very small F_∞. The point of closest approach $\hat{r}$ is nearly the critical point r^*, and the impact parameter y_{in} is also very

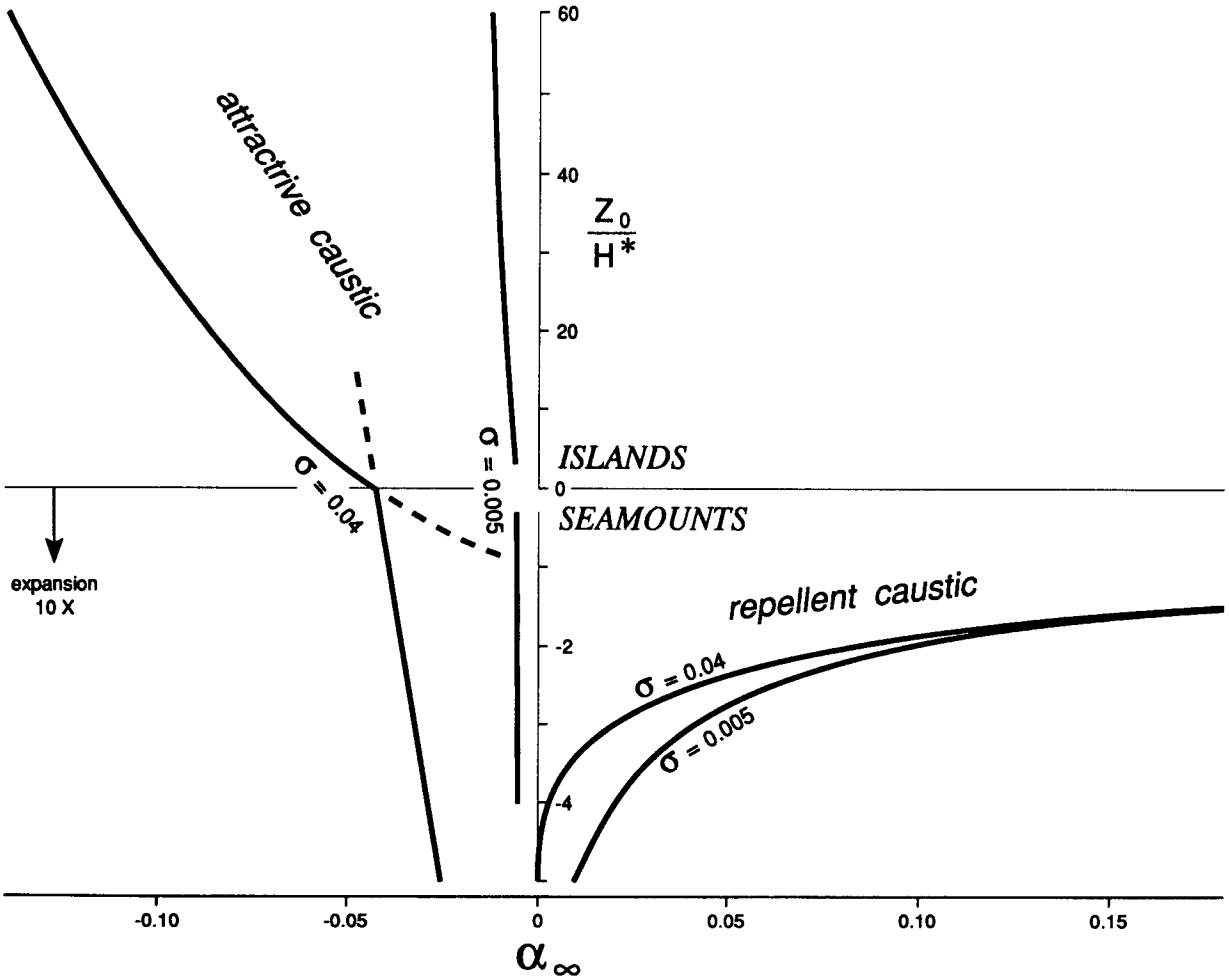

FIG. 9. Scattering angle along the attractive caustic (negative α_∞) and the repellent caustic (positive α_∞) as function of $R_0 = Z_0/H^*$, for $\sigma = 0.04$ and $\sigma = 0.005$, respectively. A break in scale between positive and negative R_0 is responsible for the apparent kinks in $\alpha_\infty(R_0)$ at $R_0 = 0$.

small. In this regime the exponential in Eq. (3) can safely be neglected, so the expression for the integrand of F_∞ reduces to

$$\left\{\left(\frac{r}{y_{\text{in}}}\right)^2\left[1 - \frac{1}{\gamma^{*2}}\frac{H^{*2}}{H(r)^2}\right] - 1\right\}^{-1/2}. \quad (32)$$

We confine ourselves to the case of a linear bottom, so that $H = \mu(r - r_0)$. (Recall $r_0 \geq 0$ for islands and <0 for seamounts.) Obviously, when $y_{\text{in}} = 0$, $F_\infty = 0$ too, so $\alpha_\infty = \pi$ as it should.

Assuming $Y \ll \hat{R}$, (12) may then be rewritten in the form

$$F_\infty = |Y| \int_{\hat{R}}^{\infty} \frac{dR}{R^2} \times \frac{R - R_0}{[(R - R_0)^2 - (R^* - R_0)^2/\gamma^{*2}]^{1/2}}. \quad (33)$$

Note that $R^* - R_0$ can be replaced by 1, using (20). This integral is readily evaluated, and we find

$$F_\infty = |Y|\left\langle \frac{R_0}{L^2}\left\{1 - \frac{[(\hat{R} - R_0)^2 - (\gamma^*)^{-2}]^{1/2}}{\hat{R}}\right\} + \frac{1}{\gamma^{*2}}\left(\frac{1}{-L^2}\right)^{3/2} \times \left(-\sin^{-1}\gamma^* R_0 - \sin^{-1}\gamma^* \frac{L^2 - R_0\hat{R}}{\hat{R}}\right)\right\rangle \quad (34a)$$

for

$$L^2 = R_0^2 - \gamma^{*-2} < 0,$$

and

$$F_\infty = |Y|\left\langle \frac{R_0}{L^2}\left\{1 - \frac{[(\hat{R} - R_0)^2 - (\gamma^*)^{-2}]^{1/2}}{\hat{R}}\right\} - \frac{1}{\gamma^{*2}}\frac{1}{L^3} \times \ln\frac{L^2 - R_0\hat{R} + L[(\hat{R} - R_0)^2 - (\gamma^*)^{-2}]^{1/2}}{\hat{R}(L - R_0)}\right\rangle \quad (34b)$$

for $L^2 > 0$. Thus, F_∞, and hence $(\pi - \alpha_\infty)/2$ varies linearly with (small) impact parameter for near backscatter, with the indicated coefficient.

To lowest order in Y, we may set $\hat{R} - R_0 = 1/\gamma^*$ on the right-hand side of Eq. (34a) and (34b), as indicated by Eq. (21) (with the exponential neglected). Therefore (34a) and (34b) may be rewritten in the simpler form

$$F_\infty = |Y|\left[\frac{R_0}{L^2} + \frac{1}{\gamma^{*2}}\left(\frac{1}{-L^2}\right)^{3/2}\left(\frac{\pi}{2} - \sin^{-1}\gamma^* R_0\right)\right] \tag{34c}$$

if $L^2 < 0$, and

$$F_\infty = |Y|\left[\frac{R_0}{L^2} + \frac{1}{\gamma^{*2}L^3}\ln\gamma^*(R_0 - L)\right] \tag{34d}$$

if $L^2 > 0$. Note that when $R_0 = 0$, (34c) reduces to $F_\infty = Y\gamma^*\pi/2$ and so $F_\infty = Y\pi/2$ for $\gamma^* = 1$, in agreement with (28). When $R_0 = -1/\gamma^*$ becomes zero, Eqs. (34) becomes singular, corresponding to the transition from backscatter to purely forward scatter as indicated in the lower panel of Fig. 6. For $\gamma^* R_0 \gg 1$, $F_\infty = Y/R_0$.

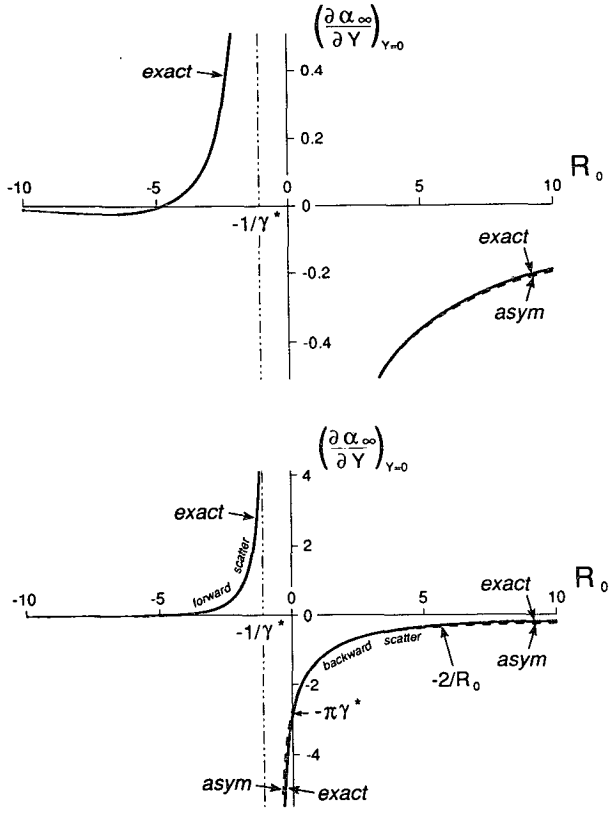

FIG. 10. Dispersion $\partial\alpha_\infty/\partial Y = -2F_\infty/Y$ at $Y = 0$ for asymptotic backscatter solution [(34c) and (34d); dashed] and the "exact" expression (27) using $[\alpha_\infty(0.04) - \alpha_\infty(0.02)]/0.02$. The agreement is too close to be plotted. The scale has been enlarged on upper panel to show negative values of $\partial\alpha_\infty/\partial Y$ for $R_0 < -5$. Note that $\partial\alpha_\infty/\partial Y \to -\infty$ as $R_0 \to -1/\gamma^*$ and $\partial\alpha_\infty/\partial Y \to -2/R_0$ for $R_0 \gg +1$.

Figure 10 shows the exact and asymptotic solutions for $d\alpha_\infty/dY = -2F_\infty/Y$ at $Y = 0$. The left branch is for forward scatter.

d. The acoustic coastline

The situation for backscatter can be modeled by reflection from a vertical cylinder. From Fig. 5 we note that near backscatter the incident ray is almost straight until it "collides" with the barrier at $R = R^*$. For a collision at azimuth α^* (Fig. 11) we have $Y = R^* \sin\alpha^*$, and

$$\alpha_\infty = \pi - 2\alpha^* = \pi - 2\arcsin(Y/R^*) \tag{35}$$

which is shown in Fig. 11 for $Z_0/H^* = 3$, $R^* = 4$. The scattering angle α_∞ compares favorably with the exact solution from $\alpha_\infty = \pi$ (backscatter) to $\frac{1}{2}\pi$. For large R_0, $\alpha_\infty \to \pi - 2YR^*$, in agreement with (34d).

One may expect a better approximation by replacing the reflecting cylinder of constant radius R^* by a reflecting wall at the radius of perigee $\hat{R}(\alpha)$ or equivalently $\hat{y}(x)$. We define two angles:

$$\tan\beta = d\hat{y}/dx, \quad \tan\chi = \hat{R}(d\alpha/dR)_{\hat{R}},$$

where $(d\alpha/dR)_{\hat{R}}$ is evaluated as in (22) but with the integrand replaced by its $\hat{R}$ derivative. The final result is

$$\alpha_\infty = 2\beta = 2(\hat{\alpha} + \chi) \tag{36}$$

which is plotted in Fig. 11 against $Y = \hat{F}\sin\hat{\alpha}$. The true curve is closer to the cylinder than to the perigee approximation.

7. Intensity

We consider a coastal reflection from a deep-water source to a deep-water receiver. Source and receiver are at $x' = \pm\frac{1}{2}d$, $y' = 0$ (Fig. 12). For any scattering point $P(x', y')$, the scattering angle is given by

$$\cos\alpha_\infty = \frac{(\frac{1}{2}d)^2 - x'^2 - y'^2}{d_{in}d_{sc}},$$

$$\begin{pmatrix} d_{in}^2 \\ d_{sc}^2 \end{pmatrix} = (x' \pm \tfrac{1}{2}d)^2 + y'^2 \tag{37}$$

where α_∞ is the total angle through which the ray is turned. The situation as shown corresponds to a repelled ray. From now on we write α for α_∞. (For larger distances, α_∞ has to be computed from spherical geometry.)

For any specified "delay" $\Delta d = d_{in} + d_{sc} - d$, the point of reflection lies on an ellipse

$$\frac{x'^2}{a^2} + \frac{y'^2}{b^2} = 1$$

with $2a = d + \Delta d$, $b^2 = a^2 - (\frac{1}{2}d)^2$.

We assume that acoustic range is large compared to the radius of the scatterer. The incident rays are then essentially parallel and separated by $\delta y_{in} = d_{in}\delta\phi$, where $\delta\phi$ is the angular ray separation at the source. Let x

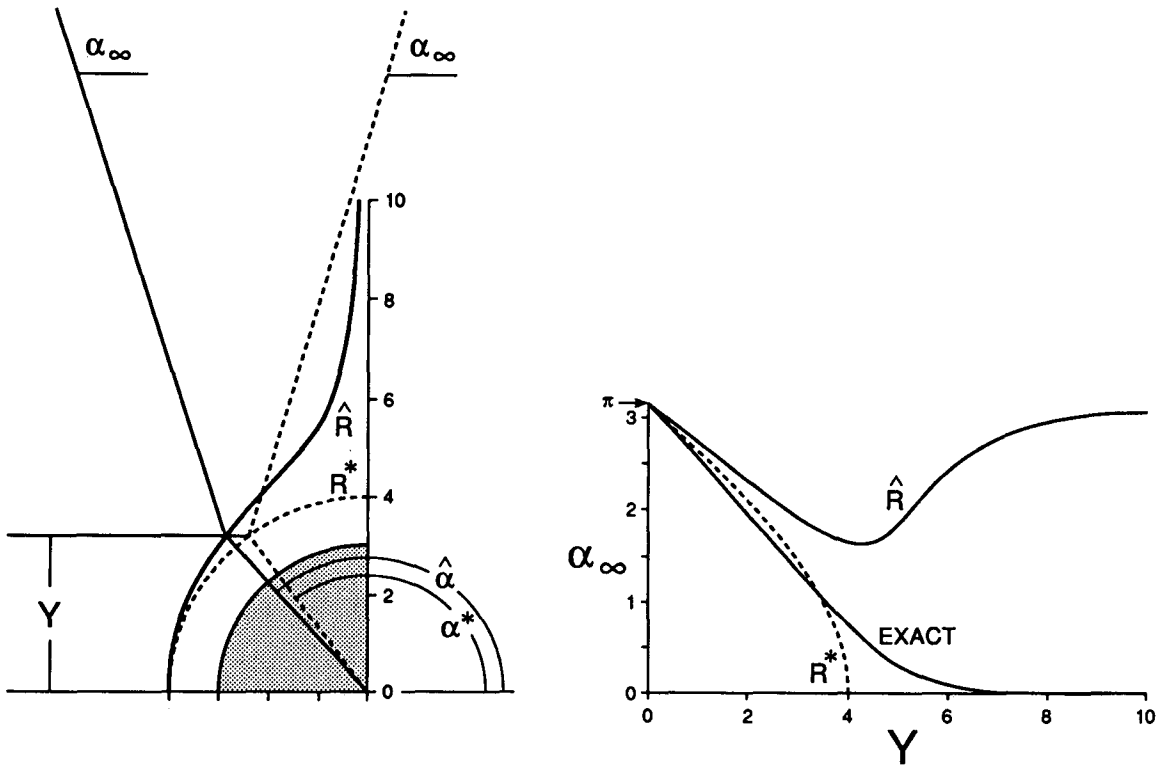

FIG. 11. Approximation for large-scale scatter (including backscatter). Left: the *refraction* diagram for the first panel of Fig. 5 ($Z_0/H^* = R_0 = 3$, $R^* = 4$) is approximated by straight rays with a *reflection* at the barrier radius R^* (dashed) and the ray perigee $\hat{R}$ (solid). Right: the scattering angle α_∞ as function of the impact parameter Y for these two cases, plus the solution given by refraction.

point in the direction of the incident ray. When reflection occurs, a ray bundle within δy_{in} is scattered into a cone of angle

$$\delta\alpha = \frac{d\alpha(y_{in})}{dy_{in}}\,\delta y, \quad \delta y_{in} = d_{in}\delta\phi, \tag{38}$$

so that, after traveling a distance d_{sc}, it is spread over a width

$$d_{sc}\delta\alpha = d_{in}d_{sc}(d\alpha/dy_{in})\delta\phi, \tag{39}$$

to be compared with a width $d\delta\phi$ for the direct transmission. The reduction in intensity due to scattering is accordingly

$$\frac{I_{sc}}{I} = \frac{d\,\delta\phi}{d_{sc}\delta\alpha} = \frac{d}{d_{in}d_{sc}}\frac{dy_{in}}{d\alpha} \tag{40}$$

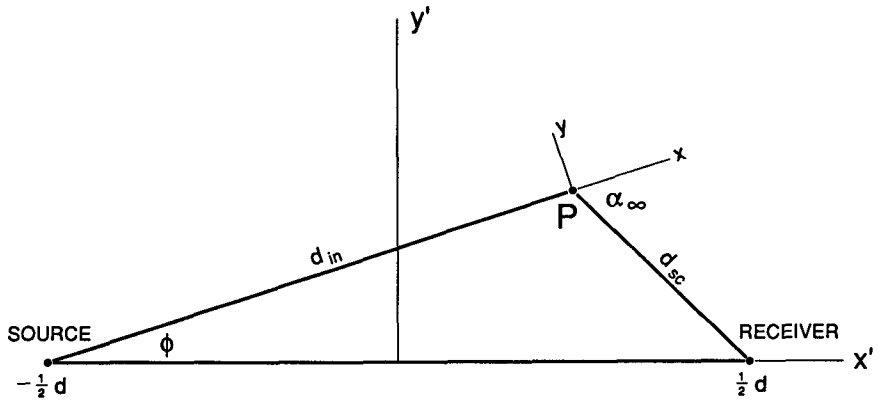

FIG. 12. Definition plot.

$$= \frac{d^2}{d_{in} d_{sc}} \frac{H^*}{\mu d} \left| \frac{dY}{d\alpha} \right| \quad (41)$$

$$= \frac{d^2}{d_{in} d_{sc}} \frac{r_0}{d} \frac{1}{R_0} \left| \frac{dY}{d\alpha} \right| . \quad (42)$$

For a given acoustic range, there are three sets of parameters:

(i) The geometric parameters d_{in}, d_{sc}, α which depend only on the location of the scatterer.

(ii) The island/seamount parameters H_0, μ, r_0.

(iii) The acoustic mode parameters N, f, which appear only through $H^* = (n + 1/2)/2fS$.

The first term in either form (41) or (42) depends only on geometric parameters (Fig. 13), and the third term is a function of α and R_0 (Fig. 7).

8. Bottom absorption

The computed intensities have to be modified to allow for bottom absorption. Acoustic waves striking the bottom at near normal incidence penetrate the bottom as seismic waves (for example, Officer 1958, p. 79). The problem has been discussed by Dashen and Munk (in preparation) as it applies to straight coast lines.

By far the most important effect of bottom absorption of sound waves occurs when the incident ray angle (relative to the bottom normal) is less than a critical angle χ_{crit} defined by

$$\sin\chi_{crit} = C_{water}/C_{rock}. \quad (43)$$

If the incident ray is less steep ($\chi > \chi_{crit}$) then there is total reflection; for steeper incidence ($\chi < \chi_{crit}$) the reflection very quickly becomes negligible (Dashen and Munk, in preparation).

For normal incidence on the island or seamount (impact parameter $y = 0$), an incident ray inclined at an angle θ relative to the horizontal and striking the bottom of slope μ, the relation is $\theta = 90° - \chi - \mu$ (Fig. 14). At the point of closest approach r^* the reflected ray is nearly vertically upwards, hence $\mu = \chi$ and

$$\theta^* = 90° - 2\mu. \quad (44)$$

For this case, the condition for absorption is simply $\mu = \chi < \chi_{crit}$, which is the case for typical islands.

The situation is more complicated for $y \neq 0$. An analytic situation is readily available for the "equivalent wall" approximation (section 6d) in which we suppose the straight ray to be reflected at a point r^*, α^* from a perfectly reflecting circular wall of radius r^* (Fig. 11), with $y = r^* \sin\alpha^*$ constant up to the point of reflection. Writing

$$\hat{n}_{bot} = \hat{e}_x \sin\mu \cos\alpha + \hat{e}_y \sin\mu \sin\alpha + \hat{e}_z \cos\mu,$$

$$\hat{n}_{ray} = \hat{e}_x \cos\theta - \hat{e}_z \sin\theta$$

yields

$$\hat{n}_{bot}\hat{n}_{ray} = \cos(\pi - \chi) = -\cos\chi$$

$$= \sin\mu \cos\theta \cos\alpha - \cos\mu \sin\theta.$$

Then for the last bounce, using $\theta = \theta^* = 1/2\pi - 2\mu$ from (44) and $\alpha = \alpha^* = 1/2(\pi - \alpha_\infty)$ from (35),

$$\cos\chi = \sin\mu \sin 2\mu \sin 1/2\alpha_\infty + \cos\mu \cos 2\mu \quad (45)$$

for $y = 0$, $\alpha^* = \pi$ (46) reduces to $\mu = \chi$, as before.

Figure 15 is plotted in accordance with (45). Take a fairly representative value of $C_{water}/C_{rock} = 1/2$. For normal incidence ($\alpha^* = 180°$) we have absorption when $\mu < 30°$ and total reflection when $\mu > 30°$. Thus, for normally existing slopes the incident energy will be absorbed. Even for fairly glancing incidence the slope required for reflection needs to exceed 15°. For very rocky coasts, with a velocity ratio of 1/3, say, the critical slopes are 17° for normal incidence and 7° for glancing incidence, and there is opportunity for total reflection. For very soft sediments the velocity ratio approaches unity, and so energy is totally absorbed even for glancing incidence. In summary, total reflection occurs for forward scattering over rocky and steep topography.

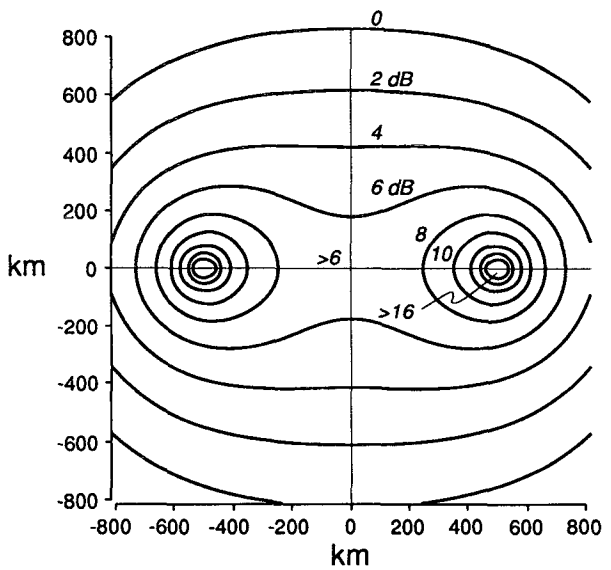

FIG. 13. A plot of 10 $\log(d^2/d_{in}d_{sc})$ for source and receiver at $x = \pm 500$ km, $y = 0$.

9. Eddies

It is interesting to compare the magnitude of horizontal refraction with that caused by mesoscale eddies. The simplest model is that of a one-dimensional horizontal refraction at the sound channel (Munk 1980), and this agrees in magnitude with a mode-theoretical calculation by Hall and Irving (1989).

We take an eddy of radius r_0, with an index of refraction

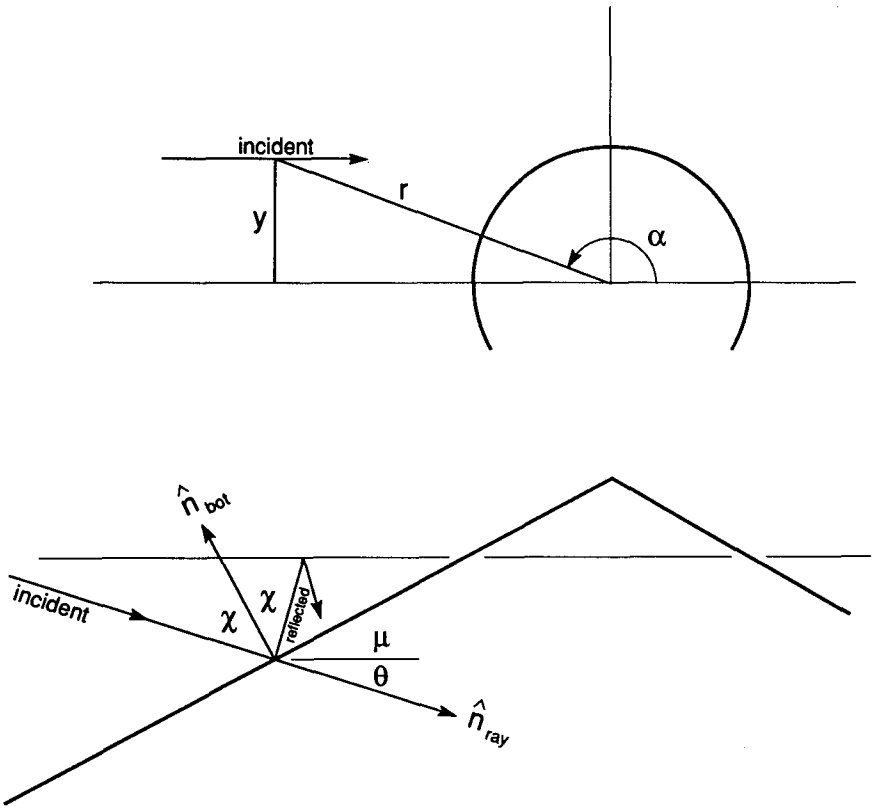

FIG. 14. Top view and a section through the island center. The incident ray enters along a straight line until it collides with the "acoustic coast line" (Fig. 11). At this point the reflected ray is nearly vertically upwards. The term $\hat{n}_{bot}$ is the unit normal to the bottom, and $\hat{n}_{ray}$ is the unit vector in the direction of the incident ray striking the bottom.

$$n(r) = S(r)S_0^{-1} = 1 + \nu \frac{r_0^2 - r^2}{r_0^2} \qquad (46)$$

for $r \leqslant r_0$ and $n = 1$ for $r > r_0$. [The results are not sensitive to the assumed form of $n(r)$.] For a typical mesoscale eddy ν is of order 0.01 ($\delta C = 15$ m s^{-1} and $\delta\theta = 3$°C at the eddy center), but may reach 0.03 for intense Gulf Stream rings; ν is positive for cold (cyclonic) eddies. The ray is bent through a total angle (Munk 1980)

$$\alpha_\infty = -4\nu \frac{y_{in}}{r_0}\left(1 - \frac{y_{in}^2}{r_0^2}\right)^{1/2} \qquad (47)$$

which has a maximum magnitude of 2ν for an impact parameter $y_{in} = r_0/\sqrt{2}$. Thus, for a warm eddy of order 3°C, α_∞ is positive (repulsive, see Fig. 3) and of order 1° or 2°.

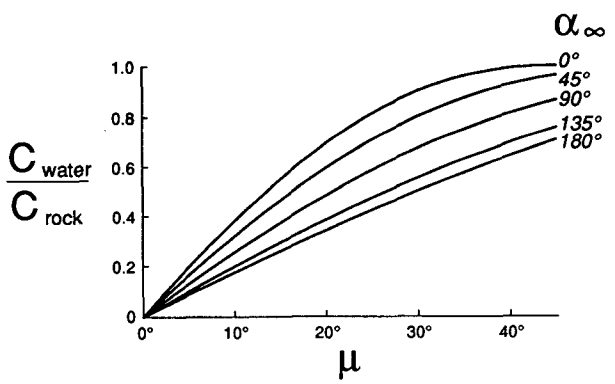

FIG. 15. The coordinates designate the geologic absorption parameters: bottom inclination μ and velocity ratio $\sin\chi = C_{water}/C_{rock}$. Lines correspond to the scattering angle α_∞ according to Eq. (45), from 0° for forward scatter to 180° for backward scatter. For any given α_∞, total reflection occurs if a point corresponding to the parameter μ, C_{water}/C_{rock} falls *beneath* the line. The construction is based on the approximation illustrated in Fig. 11 and fails near forward scatter.

Figure 16 shows the total deflection for a warm and cold eddy ($\nu = \pm 0.01$) of 100 km radius, an island of radius 50 km ($R_0 = 25$) and a seamount $R_0 = -3$, using a "realistic" $\sigma = 0.005$ (previous figures were drawn for $\sigma = 0.04$). The important points are the extrema (caustics), and here we note that a typical cold eddy attracts more strongly than the island and seamount. The opposite holds for the repulsive deflection. Here the islands and seamounts are equivalent to a very hot eddy interior. The repulsive caustic of a seamount can lead to deflections greatly exceeding those of the warm eddy.

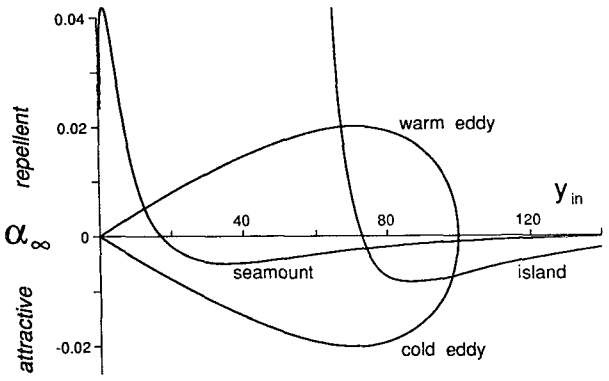

FIG. 16. Forward scattering by a warm and cold eddy of 100 km radius, and with $|\delta C| = 15$ m s^{-1} at the eddy center (see text). For comparison, we show the solution for a large island ($R_0 = 25$) and a seamount ($R_0 = -3$), using $\sigma = 0.005$.

10. Cape of Good Hope[2]

Figure 17 shows the results of a global transmission experiment conducted in 1960 (Shockley et al. 1982). When lateral sound speed gradients and the ellipticity of the earth are taken into account, there is no direct acoustic path from source to receiver. Munk et al. (1988) propose that refraction associated with the intense mesoscale activity in the area of the Agulhas retroflection may be responsible for diverting acoustic energy into the shadow zone. What is required is a deflection by 3° (Fig. 18), and this within the scope of mesoscale refraction. We had hoped that refraction around the shallow water of Cape Agulhas may offer a more plausible explanation, but the results plotted in Fig. 16 would indicate that the attractive refraction is too weak to account for the required 3° angle.

11. Bermuda double pulse[3]

We note from Fig. 17 a double pulse, trailing the principal peak by about 30 s and 10 dB. Munk et al. (1988), propose a reflection from the steep southeastern flank of Bermuda Island (Fig. 19). The travel time delay is within reason. We want to know whether the measured intensity can be accounted for. This is a case of near backscatter, and we can use the approximation of an acoustic coastal reflector. From (35) $d\alpha_\infty/dY \approx -2/R^*$. We estimate $f = 15$ Hz, mode $j = 0$, so that $H^* = C/4f = 25$ m. The slope is very steep, of order $\mu = 0.2$, and so $H^*/\mu = 125$ m. We take $r_0 = 15$ km, hence, $R_0 = 120$, and $R^* = R_0 + 1 \approx R_0$. Further, $d_{in} \approx d$. Equation (42) now greatly simplifies:

$$\frac{I_{sc}}{I} = \frac{r_0}{2d_{sc}} = -7 \text{ dB} \qquad (48)$$

for $r_0 = 15$ km, $d_{sc} = 40$ km. The numbers are of course very loose, and all one can say is that a significant scattered signal is not unexpected. The question arises why one does not receive a scattered signal from the mainland near the source? We estimate that the detonation was 150 km offshore, and that r_0 can be interpreted as the radius of curvature of the reflecting coast line. Under those circumstances the reflected signal should be much weaker.

It is assumed that bottom losses are negligible. This calls for rather extreme values of the parameters involved, such as a bottom slope of 15°, a ratio $C_{water}/C_{rock} = 1/3$, and a 90° scattering angle.

12. WIGWAM and CHASE

In 1955, during a period when numerous nuclear explosions were set off to measure various effects in various environments, a 30-kton bomb known as WIGWAM was detonated in deep water (650 m) off the coast of California. There have been no other known deep nuclear explosions, so WIGWAM constitutes, and may well remain, a singular event.

The explosion produced acoustic echoes from many islands, seamounts, and other topographic features throughout the entire Pacific Ocean, and these echoes, shown in Fig. 20, were recorded by receivers on the California coast at Point Sur and Point Arena, as well as at Kaneohe on Oahu. The source of individual acoustic peaks shown are identified by travel time and, sometimes, triangulation. As indicated in Fig. 21, all of the recorded peaks in the echo signals represent what is nearly backscatter.

For illustration we have selected two peaks, labeled Midway and Fiji, on the Point Sur record. Since the geometry is nearly backscatter, and in view of the large values of R_0 involved, we are justified in using Eq. (35) from which to an excellent approximation $d\alpha/dY = -2/R_0$ is obtained, as in the Bermuda example previously discussed. As before, then, we have a simple expression for the ratio of scattered to direct intensity at the receiver, namely,

$$\frac{I_{sc}}{I} = \frac{r_0 d}{2d_{in}d_{sc}}. \qquad (49)$$

From Fig. 20 we estimate the direct signal (in arbitrary units) to be 42 dB, that reflected from Midway to be 28 dB, and that reflected from Fiji to be 20 dB. Using these values, and the known (flat earth—since our calculations are also for a flat earth, this is sufficient for our purposes) distances and scattering angles, we can derive the necessary values of r_0 from Eq. (49): $r_0 \approx 500$ km for Fiji, and $r_0 \approx 1750$ km for Midway.

At first glance these are ridiculously large values, particularly for Midway. We must remember, however, that our calculations are for idealized conical islands and seamounts, and neither Midway nor Fiji comes close to being a simple cone. In particular, Midway is just one of many islands in a long submerged nearly linear mountain range. So r_0 does not represent the radius of an island, but is rather the local radius of

[2] Munk et al. (1988) dealt with axially refracted geodesics, using the two-dimensional field of sound speed at the sound axis. Heaney et al. (in press) have now shown that for the case of three-dimensional refraction there are, in fact, two horizontally refracted paths between Perth and Bermuda, and these nicely account for both the primary arrival and the subsequent second pulse. See also Munk (1991).

[3] See n. 2.

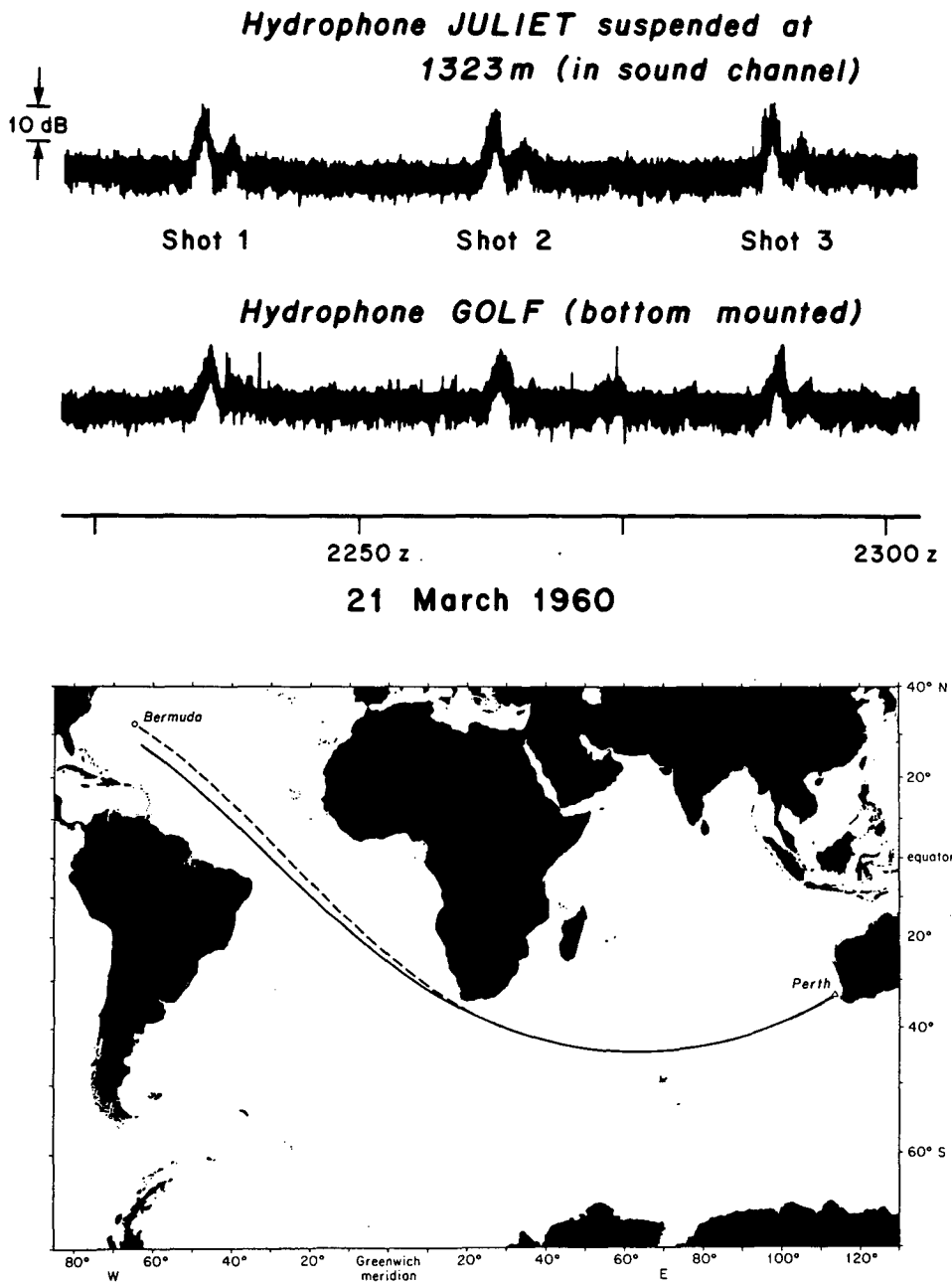

FIG. 17. Three detonations at 5-min intervals off Perth, Australia, in 1960 were clearly recorded at Bermuda half-way around the globe (adapted from Shockley et al. 1982). The refracted geodesic (which reduces to a great circle for uniform sound speed on a spherical earth) that is tangent to the Cape of Good Hope misses Bermuda (solid curve), and a scatter through a 3° angle (dashed curve, see also Fig. 15) is required to penetrate the shadow at Bermuda.

curvature of the region at which the principal acoustic reflection takes place. An inspection of the bottom contours in the region surrounding Fiji and Midway show fairly shallow areas with very large radii of curvature. For example, the 100-m depth contour along the northern shore of Vanua Levu in Fiji has a radius curvature of about 400 km; to the northeast the region near Fiji is very broken up by small islands and reefs, but again, very roughly, an average radius of curvature of 400 km for the 100-m contour is not unreasonable.

Midway is even more difficult to assess, as it lies about a third of the way from the northwest end of the Hawaiian ridge, which is overall about 2000 km long. If the effective r_0 being measured is that of the Hawaiian ridge, then the derived value of 1750 km is, perhaps, not so unreasonable. But the ridge is very irregular, and it is impossible to assign meaningful values to r_0 based on the bottom topography alone.

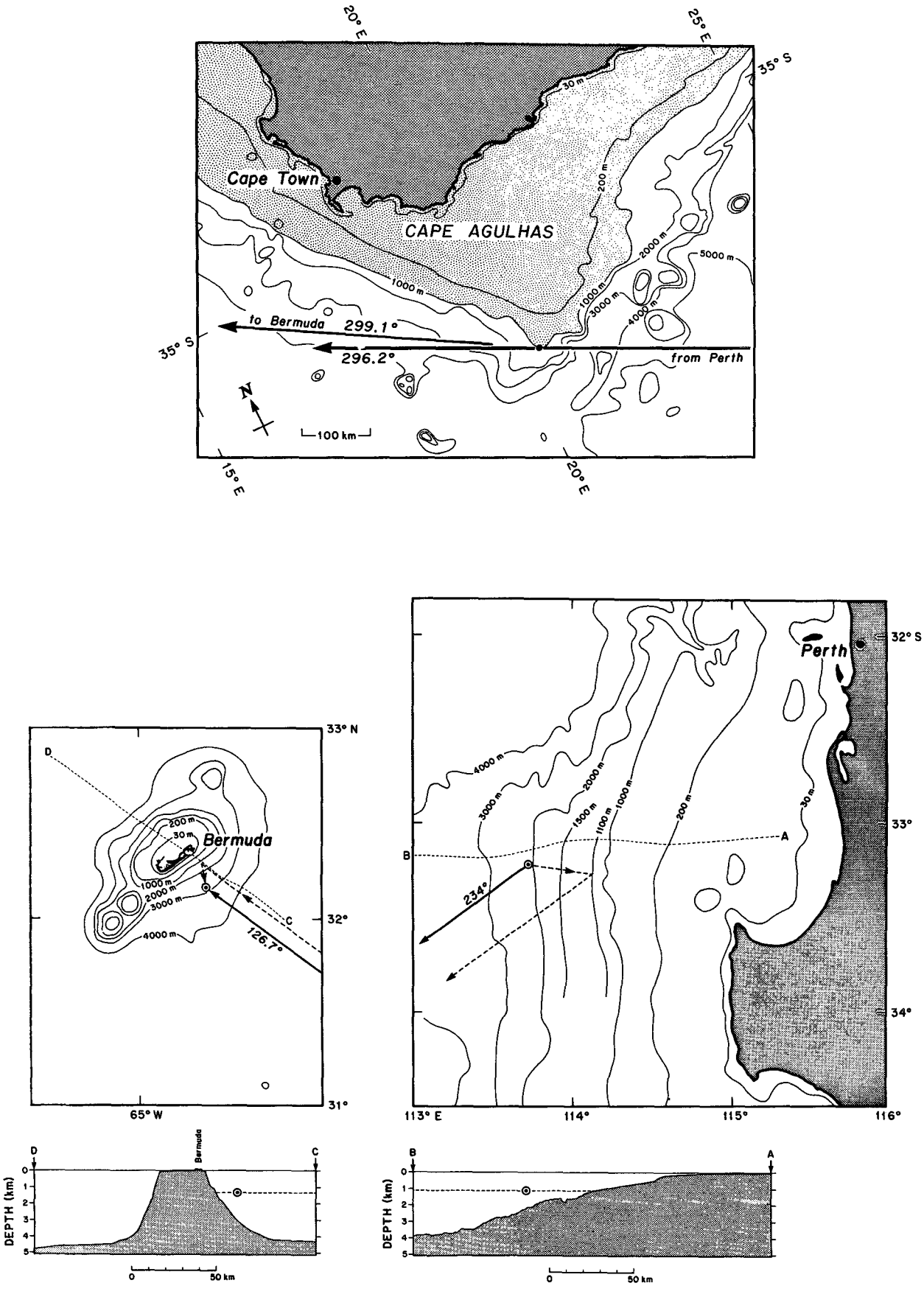

FIG. 19. Scattering geometry near the source (right) and receiver (left).

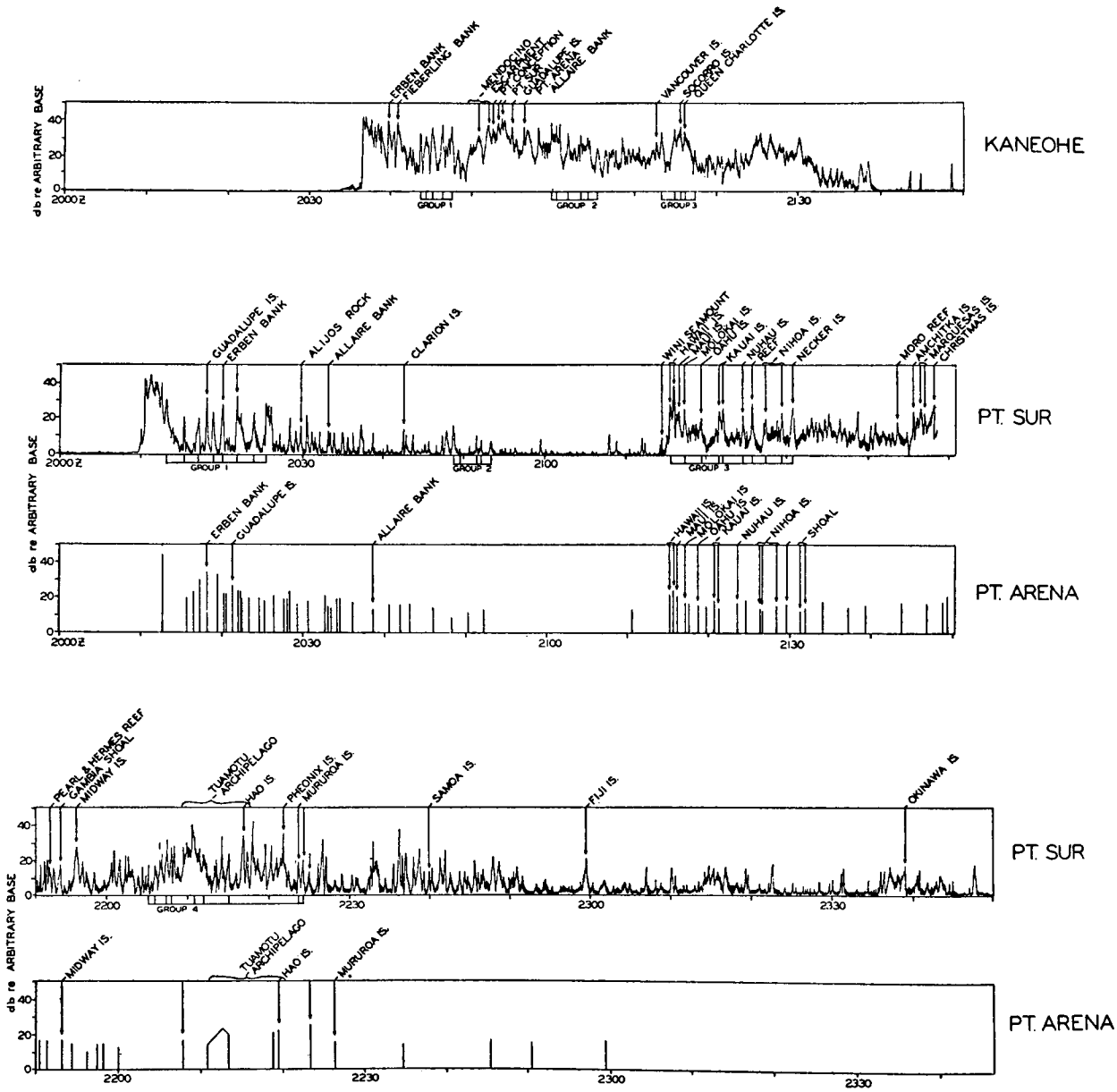

FIG. 20. The signal from WIGWAM explosion recorded at Kaneohe, Point Sur, and Point Arena (from Sheehy and Halley 1955). Identification of some of the scatterers was done by triangulation.

These estimates of reflected intensity, and the resulting values of r_0, all ignore bottom absorption, as in the Bermuda double-pulse discussion of section 11. Since Fiji and Bermuda are nearly backscatter geometries, ignoring absorption requires assuming a combination of very steep slopes and very small C_{water}/C_{rock} ratios in the region where the most important reflections take place. Such assumptions may not be totally unrealistic. The bottom topography off the island of Hawaii has been studied rather carefully (Mark and Moore 1986), and it has been found that the average slope 500 m below sea level is 13°. There are, additionally, several submarine landslides with slopes of 14°–17° for their head, which are flanked by slopes up to 19°. Altogether, the intensities measured in WIGWAM may not be so far out of line with those predicted in this paper.

Northrop (1968) reports on the CHASE (cut a hole and sink 'em) program. This involved the demolition of surplus explosives from obsolete ships. In May 1966 CHASE V was detonated off Cape Mendocino, California, at a depth of 1125 m with a yield of about 1 kton. The signal was recorded off Hawaii by hydrophones suspended from FLIP, with reverberations lasting two and a half hours after the direct arrival. The earliest reflections came from the continental slope and were −35 dB relative to the direct arrival; subsequent

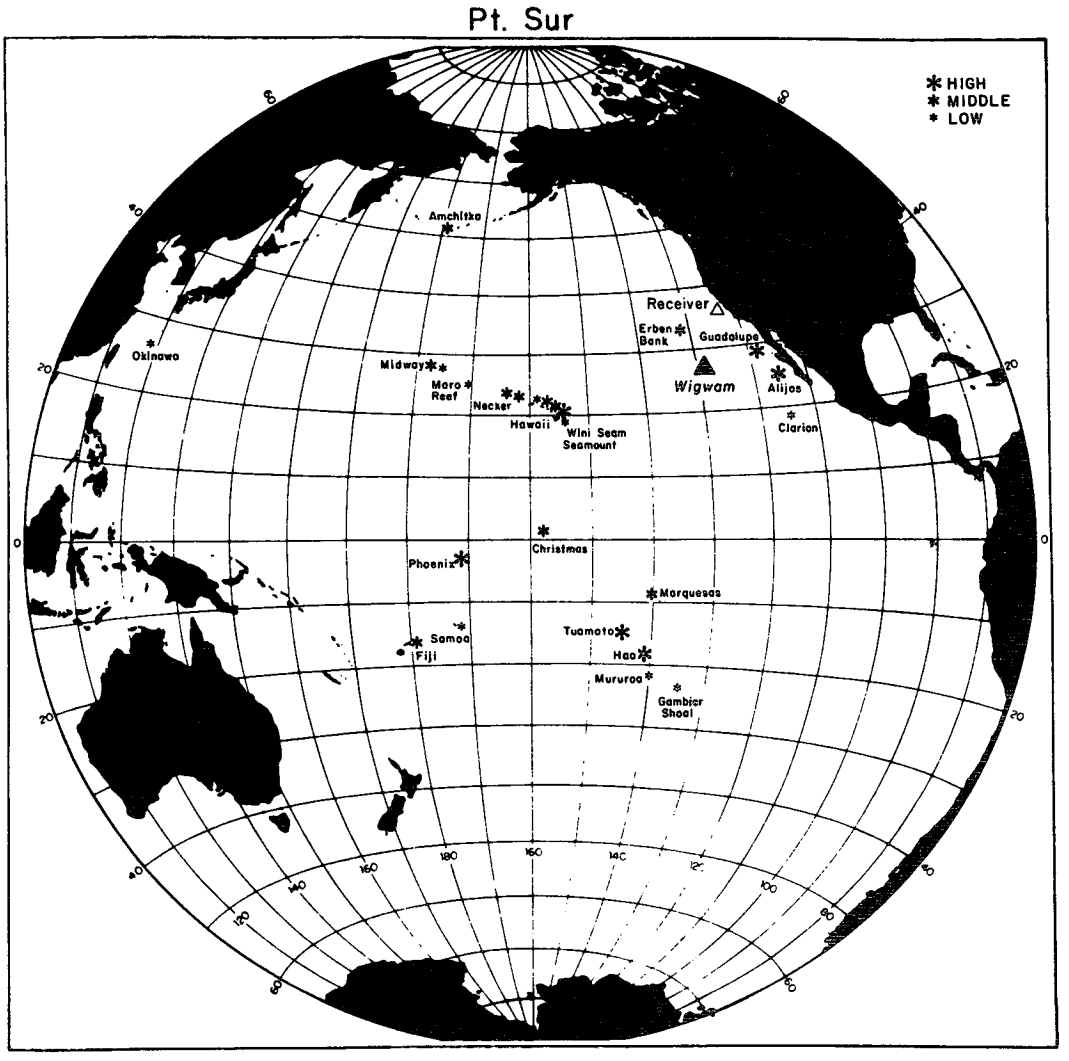

FIG. 21. Identified scatterers from the WIGWAM explosion 1955 (large triangle) are recorded at Point Sur (triangle). Location of identified scatterers are designated by stars, with size of stars indicating intensity relative to direct arrival: −4 to −14 dB, −14 to −24 dB, < −24 dB.

reflections from the Hawaiian arc were of higher intensity, up to −20 dB. Northrop remarks that the higher signal level of the Hawaiian reflections may be due to the steeper slopes and the lack of sedimentary cover (consistent with Fig. 15).

13. Conclusion

We have, in this paper, analyzed the refraction or scattering of acoustic energy by seamounts and islands, assuming a very simplified assumption of purely conical shapes with constant underwater bottom slopes. Our results can fairly be said to be both good and uncertain. The good part is that we are able to derive, both numerically and, in certain limits, analytically, predictions about scattering angles, scattered intensities, and bottom absorption. All of these results can be related rather simply to the various relevant parameters: the large-scale geometry of source, receiver, and island or seamount; the local geometry of the island or seamount; and finally the acoustic parameters (mode number and frequency). The uncertain part is that, largely because of the effects of bottom absorption, we cannot make a meaningful comparison of the computed reflected intensities with the (rather limited) available experimental information. The measured intensities in WIGWAM, CHASE, and the Bermuda experiment require large bottom slopes and small water to rock sound speed ratios.

At first glance, one might expect that our conclusions regarding absorption are mode dependent, and that some modes might suffer absorption while others are totally reflected. However, as long as the island or seamount has dimensions small compared to the distance between source and receiver, this is not true. Different

modes and different frequencies enter our formulation only insofar as they lead to different values of H^*, and therefore of R^*. But the entire geometry with which we deal simply scales with Y/R^*, so that unless there is a variation of either bottom slope μ or C_{water}/C_{rock} with depth, there is no difference between the behavior of different modes and frequencies. In this linear treatment any effect of mode coupling over the sloping bottom is ignored.

In the present formulation the properties of the sea floor appear only in the form of a planar boundary condition. The problem ought to be recast as a combined oceanography/seismology problem with a realistic island and seamount geology. One hopes that forthcoming long-range low-frequency acoustic transmissions recorded on ocean hydrophones and coastal seismic stations may provide further clues. We suggest a complementary relation between the intensities from an underwater explosion as recorded on axial hydrophones and on nearby land seismometers, with conditions favorable to reflection favoring hydrophones and vice versa.

Acknowledgments. A preliminary draft of this paper was prepared during the JASON Summer Study 1989 as part of an examination of acoustic detection of global ocean warming; F.Z. acknowledges the support of the Department of Energy. W.M. holds the Secretary of the Navy Research Chair in Oceanography.

REFERENCES

Brekhovskikh, L., and Y. Lysanov, 1982: *Fundamentals of Ocean Acoustics.* Springer, 250 pp.

Buckingham, M. J., 1986: Theory of acoustic propagation around a conical seamount. *J. Acoust. Soc. Am.,* **80,** 265–277.

Dashen, R., and W. H. Munk, 1990: A model of ocean noise. *J. Acoust. Soc. Am.,* submitted.

——, S. A. S. Jones and P. N. Harriman, 1986: Stationary phase evaluation of the integral for the acoustic field around a conical seamount. *J. Acoust. Soc. Am.,* **80,** 278–281.

Doolittle, R., A. Tolstoy and M. Buckingham, 1988: Experimental confirmation of horizontal refraction of cw acoustic radiation from a point source in a wedge-shaped ocean environment. *J. Acoust. Soc. Am.,* **83,** 2117–2125.

Hall, M. V., and M. A. Irving, 1989: Application of adiabatic mode theory to the calculation of horizontal refraction through a mesoscale eddy. *J. Acoust. Soc. Am.,* **86,** 1465–1477.

Harrison, C. H., 1977: Three-dimensional ray paths in basins, troughs, and near seamounts by use of ray invariants. *J. Acoust. Soc. Am.,* **62,** 1382–1388.

Heaney, K., W. A. Kuperman and B. E. McDonald, 1991: Perth–Bermuda sound propagation (1960): Adiabatic mode interpretation. *J. Acoust. Soc. Am.,* in press.

Luskin, B., M. Landisman, G. B. Tirey and G. R. Hamilton, 1952: Submarine topographic echoes from explosive sound. *Bull. Geol. Soc. Am.,* **63,** 1053–1068.

Mark, R. K., and J. G. Moore, 1986: United States Geological Survey Professional Paper 1350.

McDaniel, S., 1982: Mode coupling due to interaction with the seabed. *J. Acoust. Soc. Am.,* **72,** 916–923.

Munk, W., 1980: Horizontal deflection of acoustic paths by mesoscale eddies. *J. Phys. Oceanogr.,* **10,** 596–604.

——, 1991: Refraction of sound waves at polar latitude. *J. Geophys. Res.,* **96,** 1015–1022.

——, W. C. O'Reilly and J. L. Reid, 1988: Australia–Bermuda sound transmission experiment (1960) revisited. *J. Phys. Oceanogr.,* **18,** 1876–1898.

——, and A. M. G. Forbes, 1989: Global ocean warming: An acoustic measure? *J. Phys. Oceanogr.,* **19,** 1765–1778.

Northrop, J., 1968: Submarine topographic echoes from CHASE V. *J. Geophys. Res.,* **73,** 3909–3916.

Officer, C. B., 1958: *Sound Transmission.* McGraw-Hill, 284 pp.

Sheehy, M. J., and R. Halley, 1955: Measurement of attenuation of low-frequency underwater sound. *J. Acoust. Soc. Am.,* **29,** 464–469.

Shockley, R. C., J. Northop, P. G. Hansen and C. Hartdegen, 1982: SOFAR propagation paths from Australia to Bermuda: Comparison of signal speed algorithms and experiments. *J. Acoust. Soc. Am.,* **71,** 51–60.

Weinberg, H., and R. Burridge, 1974: Horizontal ray theory for ocean acoustics. *J. Acoust. Soc. Am.,* **55,** 63–79.

Weston, D. E., 1961: Horizontal refraction in a three-dimensional medium of variable stratification. *Proc. Phys. Soc. Lond.,* **78,** 46–52.